WHEELS OF FIRE. II. NEUTRAL HYDROGEN IN THE CARTWHEEL RING GALAXY

JAMES L. HIGDON[1,2]
National Radio Astronomy Observatory,[3] Array Operations Center, 1003 Lopezville Road, P.O. Box 0, Socorro, NM 87801
Received 1995 November 16; accepted 1996 March 6

ABSTRACT

The VLA was used to investigate the distribution and kinematics of neutral hydrogen, and the relation between massive star formation (MSF) and gas surface density, in the Cartwheel ring galaxy. Over 85% of the Cartwheel's H I resides in the outer ring, with a low surface density component filling much of the interior. Analysis of the H I velocity field indicates that the outer ring is expanding at $V_{exp} = 53 \pm 9$ km s^{-1}, and that ~ 300 Myr have elapsed since the intruder's passage. Changes in V_{exp} with radius show that gas is beginning to leave the outer ring and is infalling for $R \lesssim 8$ kpc. H I is accumulating just beyond the inner ring, though optical $(V - R)$ maps show gas and dust crossing the ring and flowing into the nucleus along two streams. No H I analogs of the optical "spokes" are found.

The ring's surface brightness in Hα ($\Sigma_{H\alpha}$) and 20 cm continuum ($\Sigma_{20\,cm}$) are identical, showing that peculiar extinction is not responsible for the observed crescent of MSF. Only the two most luminous H II complexes are detected at 6 cm and are characterized by nonthermal spectra ($\bar{\alpha} = -0.65$) and low 6 cm–Hα extinction ($\bar{A}_V = 1.7$ mag). The 20 cm continuum–derived Type II SN rate (0.1 ± 0.02 yr^{-1}) is consistent with the lower bound of optical estimates. H I and Hα are both concentrated and anti-correlated in the outer ring. MSF appears to take place on the H I ring's leading edge throughout the starburst quadrant, where a disturbed H I component is found. The Cartwheel's gas consumption time-scale is 290 Myr. If the inner ring triggers a second sustained starburst, a significant fraction of the remaining gas supply may be converted into stars.

The global distribution of MSF can be understood in terms of a critical surface density (Σ_{crit}; reported by Kennicutt in 1989): Only in the outer ring does the atomic gas surface density (Σ_{ag}) exceed Σ_{crit} when averaged over a full range in azimuth. At smaller radii, $\Sigma_{ag}/\Sigma_{crit} \leq 0.5$. The absence of strong shocks in the outer ring argue against MSF induced by high-velocity cloud collisions (as discussed by Olson & Kwan in 1990). The ring starburst appears to be the result of very massive cloud complexes formed through agglomeration at low velocities. Feedback and systematic variations in collision rates/speeds likely influence MSF on $\sim$kiloparsec scales in the ring itself. Large departures from Schmidt law behavior are found.

H I is detected in two companion galaxies. Mass estimates using their H I line widths yield values $\lesssim 6\%$ of the Cartwheel's disk + halo. A broad and massive (2×10^9 $M_\odot$) H I plume projects 82 kpc from the ring to the northeast. It is argued that this H I "splash" resulted from the passage of G3 through the Cartwheel's disk ~ 300 Myr ago. Much of this material will escape the ring galaxy.

Subject headings: galaxies: individual (Cartwheel) — galaxies: interactions — galaxies: ISM — galaxies: kinematics and dynamics — galaxies: stellar content — radio lines: galaxies

1. INTRODUCTION

The strong compression experienced by the ISM in the orbit crowded rings of collisional ring galaxies is expected to result in enhanced star formation rates (SFR) (Appleton & Struck-Marcell 1987, hereafter ASM). Many ring galaxies are thus candidates for highly extended density wave triggered starbursts ($D_{ring} = 10$–40 kpc), where the greatly reduced levels of extinction and background emission offer a privileged view of this process. Because of its large angular and physical size, high SFR, and wealth of structure, the Cartwheel is the archetype of this class of interacting system (Fig. 1). Optical emission-line studies have shown its 33 kpc diameter outer ring to be experiencing a moderate starburst (SFR = 67 $M_\odot$ yr^{-1}; $H_0 = 100$ km s^{-1} Mpc^{-1}), with 80% of this activity restricted to a single ring quadrant (Higdon

1995, hereafter Paper I). No massive star formation (MSF) was detected in the Cartwheel's nucleus, inner ring, disk, or the network of "spokes" that bridge the inner and outer rings above 2.4 $M_\odot$ Gyr^{-1} pc^{-2} (3 σ), a rate comparable to the disks of early galaxies (Caldwell et al. 1991). On the other hand, evidence was found for the direct triggering of MSF by the outer ring. The systematic variations in emission-line properties around its circumference can be attributed to changes in the mean age, age spread, or IMF of the embedded stellar populations. Estimates of the Type II SN rate based on the implied numbers of OB stars are as high as ~ 1 yr^{-1} (Fosbury & Hawarden 1977, hereafter FH). The Cartwheel is accompanied by three companion galaxies with $\Delta V_{sys} \lesssim 400$ km s^{-1} of the ring's (Taylor & Atherton 1984; FH). These have been labeled G1, G2, and G3 in Figure 1. Collectively, the four galaxies will be referred to as the Cartwheel Group.

The Cartwheel Group is gas rich,[4] providing an excellent opportunity to study the H I structure and kinematics of a large and evolved ring galaxy and to probe the MSF–

---

[1] NRAO Jansky Fellow.

[2] Present address: Australia Telescope National Facility, Paul Wild Observatory, Locked Bag 194, Narrabri, NSW, 2390, Australia; jhigdon@atnf.csiro.au.

[3] The National Radio Astronomy Observatory is a facility of the National Science Foundation operated under cooperative agreement by Associated Universities, Inc.

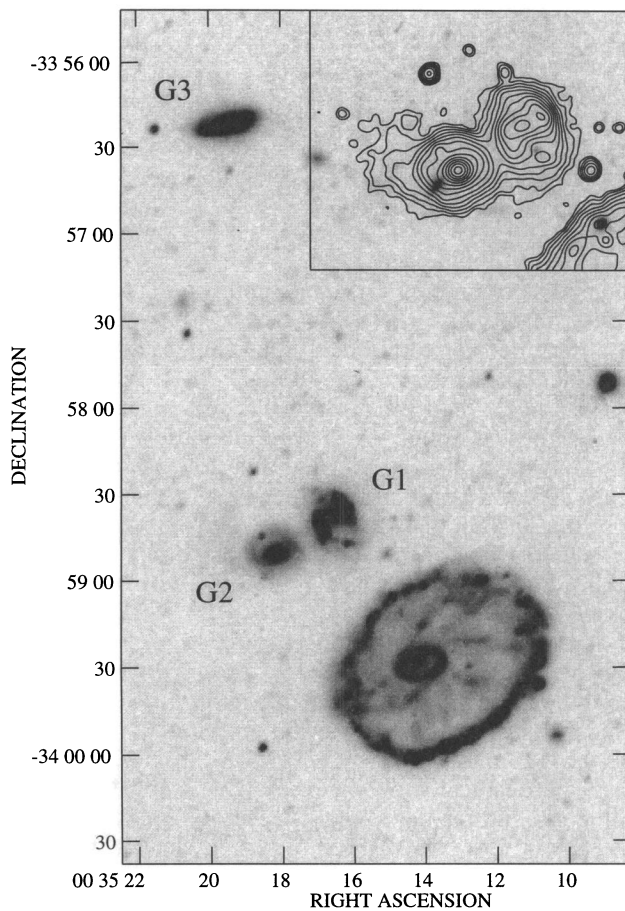[4] $M_{H I} = (1.9 \pm 0.2) \times 10^{10}$ $M_\odot$ within a 7" FWHM beam (Mebold, Goss, & Fosbury 1977).

Fig. 1.—Digitized CTIO 4 m prime focus plate (V. Blanco) showing the four galaxies of the Cartwheel Group (IIIa-J + GG385 filter; $\lambda_{eff} = 4400$ Å). The insert shows optical surface brightness contours for companion galaxies G1 and G2 using a smoothed (3″ FWHM) stack of B-, V-, R-, and I-band CCD frames. The contours are in steps of 0.4 mag arcsec^{-2} starting at $\mu_V = 25.4$ mag arcsec^{-2}. While a faint tidal feature is visible east of G2, no bridge is apparent between the Cartwheel and either companion.

and bridges that are valuable in reconstructing the collision history (see, e.g., Wallin & Struck-Marcell 1994). The discovery of such features in the Cartwheel Group could conceivably lead to the identification of the intruder galaxy responsible for the ring's genesis. Finally, the large numbers of OB stars implied by the Cartwheel's $L_{H\alpha}$ should generate measurable radio continuum flux. The nonthermal emission would provide an independent estimate of the supernova rate in the ring starburst, as well as an extinction free tracer of MSF. Thermal continuum emission can be combined with Hα fluxes to yield A_V in the H II region complexes.

The radio and optical observations, data reduction, and analysis will be described in § 2. The observational results are presented in § 3 and are discussed in more detail in § 4. This is followed by a brief summary in § 5.

2. OBSERVATIONS AND DATA REDUCTION

2.1. *Neutral Hydrogen*

The Cartwheel Group was observed for a total of 36 hr in three different array configurations to provide sensitivity to emission structures from 5″ (2.2 kpc) to several arcminutes (> 80 kpc). A listing of the instrumental parameters for each configuration is shown in Table 1. Because of the target's low declination ($\delta = -33°9$), arrays with extended north arms (i.e., BnA, CnB, and DnC) were used to provide nearly circular synthesized beams. The flux density scale was set using 3C 48 as a standard ($S_{1378.7 \text{ MHz}} = 16.13$ Jy; Baars et al. 1977). Twenty-six minute scans centered on the Cartwheel's nucleus were interleaved with 4 minute scans of $0023-263$ ($S_{1378.7 \text{ MHz}} = 8.71$ Jy), allowing the antenna gain and phase constants to be determined during the observations. Phase and amplitude variations across the bandpass were removed using two 15 minute scans of 3C 48 situated at the beginning and end of each night's observation. Strong background continuum sources within the primary beam were removed from the data prior to making the final sets of maps by subtracting a CLEAN-component model. All calibration, editing, and mapping of the UV data were done using NRAO's Astronomical Image Processing System (AIPS).

Data from the three array configurations were combined into a single database. Naturally weighted map cubes were made with a range in radial velocity from 8545.9 to 9574.2 km s^{-1} in increments of 21.9 km s^{-1}, and a synthesized beam of 10″7 × 8″4 FWHM (4.7 × 3.7 kpc). The velocity resolution in the BnA data is 42 km s^{-1}, as off-line Hanning smoothing was employed. In the analysis, each cube was smoothed in velocity to this value. A mean continuum map formed by averaging 16 line-free channels on either side of the H I profile was subtracted from the original cube to create a set of channel maps containing only H I emission. These maps were CLEANed (Clark 1980). The 1 σ noise level in the final set of maps is 0.29 mJy beam^{-1}, which was close to the expected levels. For convenience, the combined BnA + CnB + DnC data will be denoted "BCD" in the following sections. The BCD channel maps are shown in Figure 2, with the positions of the four galaxies in the Cartwheel Group indicated by crosses.

The BnA UV data were also processed separately in an identical manner. A set of naturally weighted maps were made to provide a higher resolution view (6″0 × 5″1 FWHM; 2.6 × 2.2 kpc) of H I in the system. The 1 σ map noise (0.4 mJy beam^{-1}) was again near the expected level.

neutral ISM relationship in a system clearly experiencing an extended starburst. This paper presents an H I and radio continuum study of the Cartwheel carried out using multiple configurations the Very Large Array (VLA) radio telescope. Optical $BVRI$ and Hα (Paper I) CCD images have been included to compare the galaxy's radio emission with the distributions of massive star-forming complexes, evolved stars, and dust. One of the primary questions to be addressed concerns the global distribution of star formation: Can the apparent lack of MSF over the Cartwheel's interior be attributed to the removal of this region's gas through the "intruder" galaxy's passage, or has most of the H I been concentrated in the outer ring, leaving the average gas density at smaller radii below a threshold value for spontaneous star formation (i.e., Kennicutt 1989)? Conversely, does the enhancement in MSF throughout the outer ring's southern quadrant arise from a greater concentration of H I? Is H I associated with the large stellar amplitude inner ring or the spokes? If they *are* gas rich, what is suppressing MSF? Second, since optical line emission is found only in the outer ring, an extended H I component would lead to a better understanding of ring galaxy kinematics, enabling comparisons with detailed models (see, e.g., Struck-Marcell & Higdon 1993, hereafter SMH). Third, interacting systems routinely show large-scale H I plumes

TABLE 1

INSTRUMENTAL PARAMETERS: H I OBSERVATIONS

	ARRAY CONFIGURATION		
PARAMETER	BnA	CnB	DnC
Observation dates	1991 Oct 10–11, 14	1988 Feb 19–21	1988 Jun 17–18
Shortest spacing (km)	0.20	0.060	0.045
Largest spacing (km)	22.8	5.8	2.2
R.A.$_{Field Center}$[a]	00 35 14.32	00 35 14.32	00 35 14.32
Decl.$_{Field Center}$[a]	−33 59 27.1	−33 59 27.1	−33 59 27.1
Central velocity (km s^{-1})[b]	9071.0	9071.0	9071.0
Velocity coverage (km s^{-1})	1338	1338	1338
Channel separation (km s^{-1})	21.9	21.9[c]	21.9[c]
Primary beam (FWHM) (arcmin)	31.5	31.5	31.5
Synthesized Beam (FWHM) (arcsec × arcsec)......	6.0 × 5.1	17.6 × 14.1	55.5 × 59.0
Flux/Bandpass calibrator...........................	3C 48	3C 48	3C 48
Phase/Gain calibrator	0023−263	0023−263	0023−263
Time on-source (hr)	13.5	13.5	9.0
1 σ map noise (mJy beam^{-1})[d]	0.4	0.4	0.8

NOTE.—Units of right ascension are hours, minutes, and seconds, and units of declination are degrees, arcminutes, and arcseconds.

[a] B1950.0 coordinates.
[b] Velocity and frequency are related through the optical-heliocentric definition.
[c] On-line Hanning smoothing.
[d] Noise per channel with natural weighting.

2.2. Radio Continuum

Naturally weighted 20 cm continuum maps of the Cartwheel Group were made by averaging 16 line-free channel maps in both map cubes, yielding an effective bandwidth of 1.56 MHz. Sources in both BCD and BnA 20 cm maps were CLEANed using the appropriate average beam. The 1 σ map noises were 150 and 140 μJy beam^{-1}, respectively.
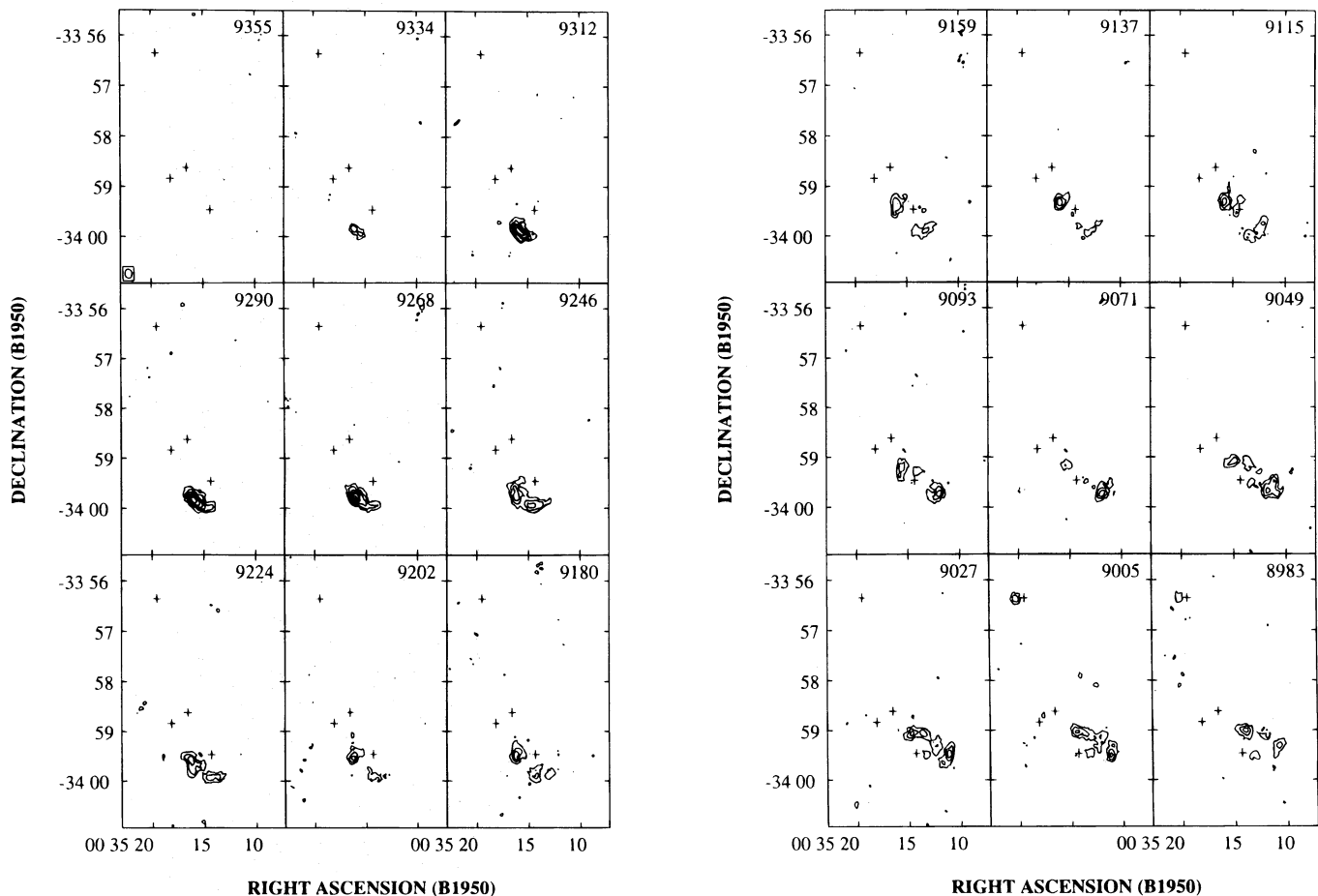
The Cartwheel Group was observed at 6 cm in the CnB

FIG. 2.—BCD H I channel maps (10″7 × 8″4 FWHM). Central velocities (km s^{-1}, optical/heliocentric) are shown at the top right of each frame. The contours are 3, 5, 7, 9, 11, and 13 times the 1 σ noise in a single channel (0.29 mJy beam^{-1}). Crosses mark the nuclei of the Cartwheel and three companion galaxies.
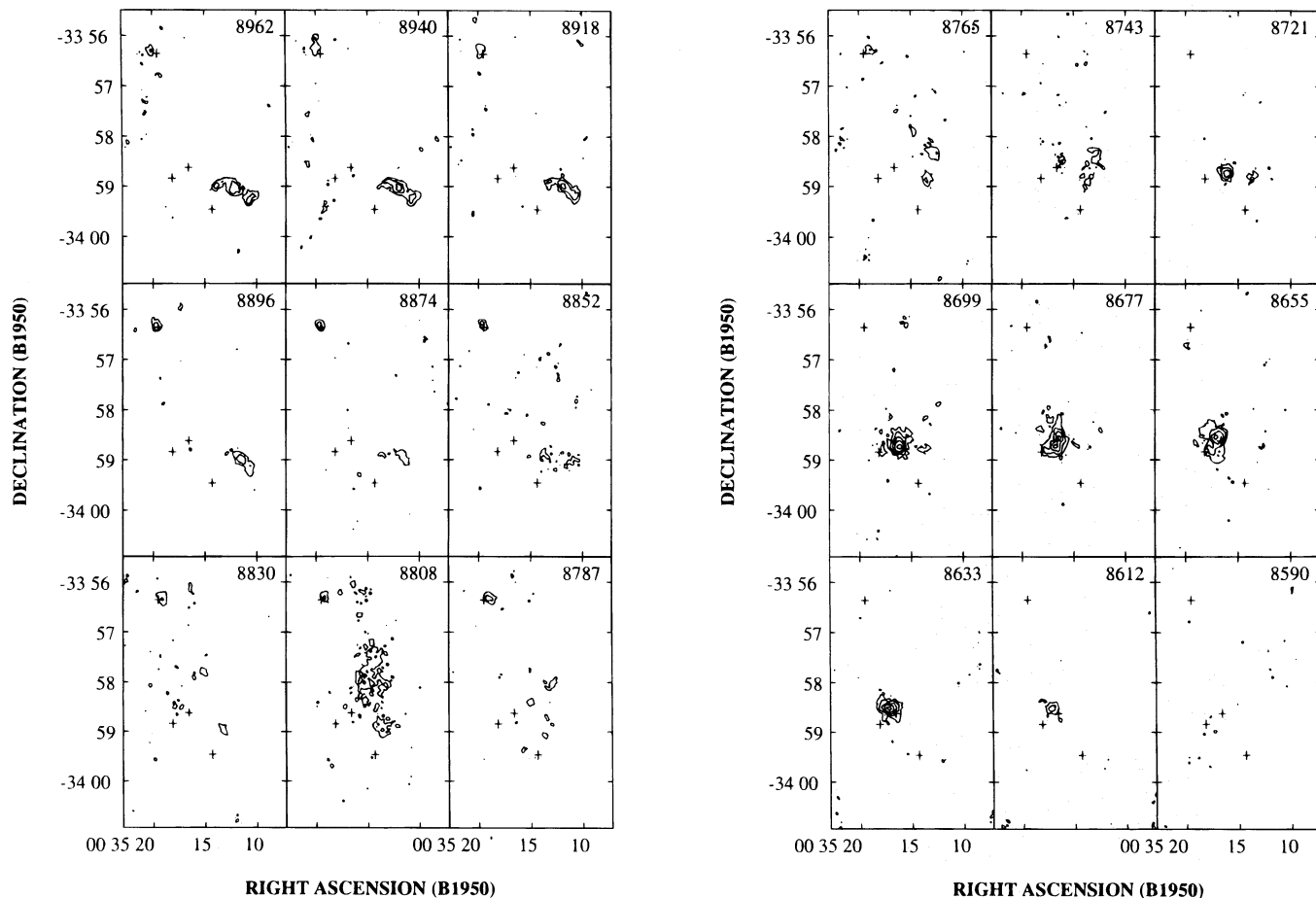
Fig. 2—*Continued*

configuration on 1988 February 27 (Table 2). This provided scaled array data in conjunction with the BnA 20 cm observations. Two independent polarizations were measured, each with a 50 MHz passband. Flux density and phase calibration were carried out using 3C 48 ($S_{4730\ MHz} = 5.41$ Jy; Baars et al. 1977) and $0008-264$ ($S_{4730\ MHz} = 0.45$ Jy). A naturally weighted map ($6\rlap{.}''0 \times 5\rlap{.}''1$ FWHM) was produced and CLEANed. The $1\ \sigma$ noise level in the final map is 75 μJy beam^{-1}, which was a factor of 2 higher than expected.

2.3. *Optical Imaging*

Broadband B, V, R, and I images of the Cartwheel and two nearest companions were obtained with the McDonald Observatory 0.76 m telescope on 1989 September 25, 27, and 28. The imaging array was a Texas Instruments 800×800 pixel CCD, operated in 2×2 co-add mode, which provided a $0\rlap{.}''58$ pixel^{-1} scale, and a $3\rlap{.}'8 \times 3\rlap{.}'8$ field of view. Filters were chosen to match the Kron-Cousins photometric system (Bessel 1979). The intrinsic seeing was better than $1\rlap{.}''5$, and the nights were photometric. Calibration was carried out by repeated observations of the $BVRI$ standard field in M92 (Christian et al. 1985) over a wide range in airmass (1.1–2.1) each night. The basic reduction and calibration was routine. Hα and off-line red continuum maps of the Cartwheel Group were also obtained using the McDonald Observatory 0.76 m telescope. For a discussion of the reduction and calibration, see Paper I. Positions of stars in the field were measured using the University of Texas Photodensitometer astrometry system (Benedict & Shelus 1978) and were used to attach a coordinate system to the optical images. The radio-optical overlay is accurate to at least $1''$.

2.4. *Data Analysis*

Two variants of the BCD and BnA map cubes were made using the interactive blanking capabilities of AIPS. One

TABLE 2
INSTRUMENTAL PARAMETERS: 6 CENTIMETER OBSERVATIONS

Parameter	Value
Array configuration	CnB
Observation dates	27 Feb 88
Shortest spacing (km)	0.060
Largest spacing (km)	5.8
R.A.$_{Field\ Center}$	00 35 14.32
Decl.$_{Field\ Center}$	$-33\ 59\ 27.1$
Total bandwidth	100 MHz
Primary beam (FWHM) (arcmin)	9.5
Synthesized beam (FWHM) (arcsec $\times$ arcsec)[a]	5.0×4.2
Flux calibrator	3C 48
Phase/Gain calibrator	$0008-264$
Time on-source (hr)	4.5
$1\ \sigma$ map noise[b]	75 μJy beam^{-1}

NOTE.—Units of right ascension are hours, minutes, and seconds, and units of declination are degrees, arcminutes, and arcseconds.

[a] Natural weighted map.
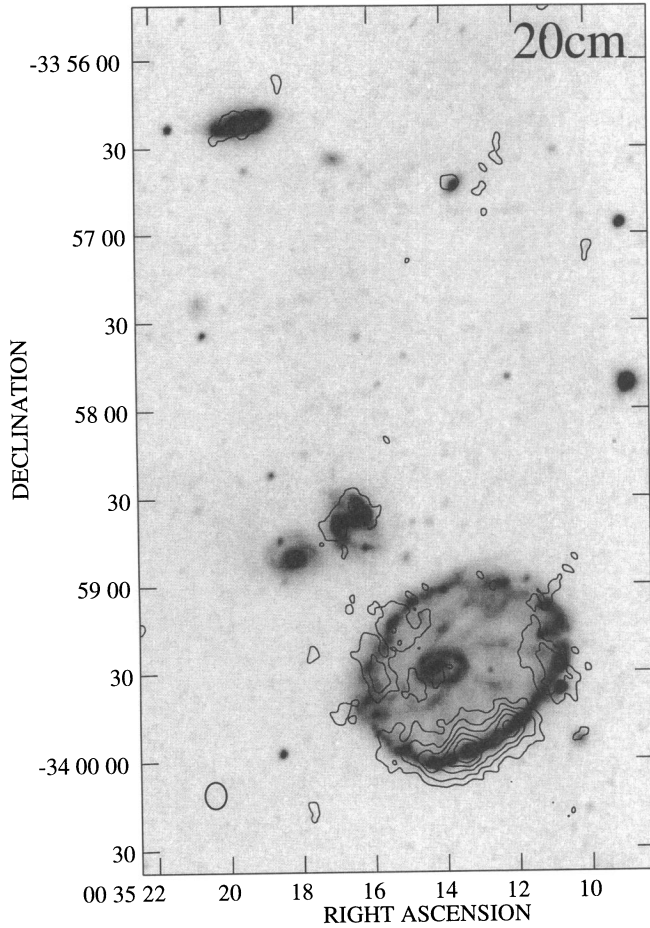
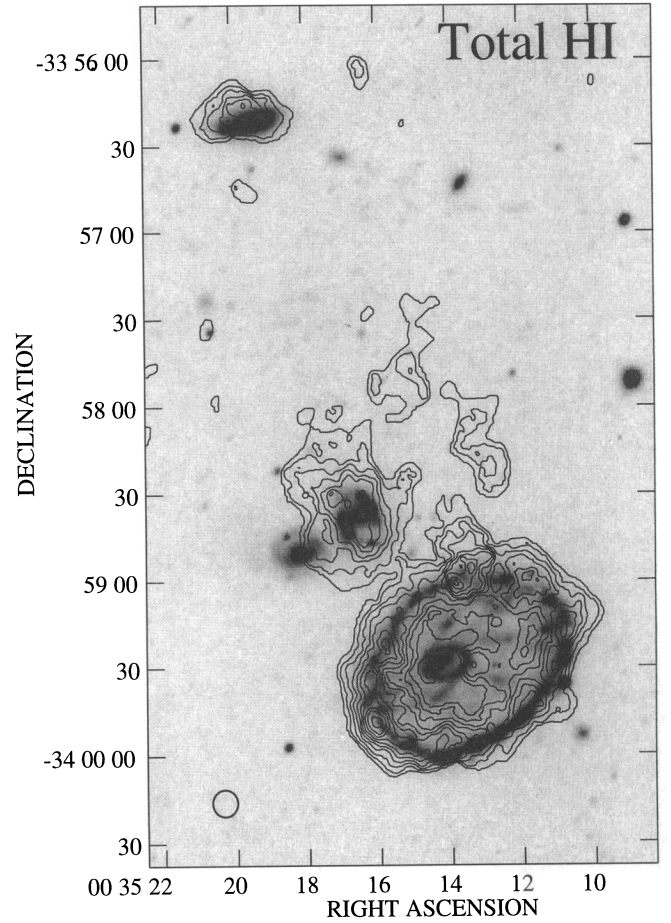[b] Noise per channel with natural weighting.

FIG. 3a

FIG. 3b

FIG. 3.—Global radio emission in the Cartwheel Group using the BCD data. (a) 20 cm continuum. Contours are 3, 5, 7, 9, 11 times 0.15 mJy beam^{-1}, the map 1 σ. (b) Integrated H I. Contour levels correspond to 1, 4, 7, 10, 13, 16, 19, 22, 25, and 28 $M_\odot$ pc^{-2}. The contours are superposed on the CTIO 4 m prime focus image.

TABLE 3

PROPERTIES OF CARTWHEEL GROUP GALAXIES

Parameter	Cartwheel	G1	G2	G3	Plume
V_{sys} (km s^{-1})	9089	8667	9080	8874	8808
H I width$_{FW\,20\%}$ (km s^{-1})[a]	481	109	115	252	~ 80
H I mass (10^9 $M_\odot$)	9.3	2.7	<0.01	0.7	3
M_{ind} (10^9 $M_\odot$)[b]	340	11	12[c]	26	...
M_{HI}/M_{ind}	0.03	0.25	<0.001	0.02	...
Peak Σ_{HI} ($M_\odot$ pc^{-2})	29	17	<0.2	15	3
H I diameter (kpc)[d]	39.5	21.1	...	14.5	65
Optical diameter (kpc)	33.0	12.7	9.1	12.8	...
20 cm flux (mJy)	11.5	1.4	<0.2	0.9	...
6 cm flux (mJy)	2.3	<0.15	<0.15	...	...
M_B[e]	−20.94	−19.02	−18.72	−19.16	...
$B-V$	0.46	0.36	0.98	...	...
log $L_{H\alpha}$ (ergs s^{-1})[f]	42.87	41.26	...	41.38	...
τ_{gas} (Gyr)[g]	0.29	2.1	...	0.8	...

[a] Uncorrected for inclination.
[b] Computed after Balkowski 1973 with ΔV corrected for inclination.
[c] Davies & Morton 1982, using optical velocity dispersion.
[d] Major axes at $\Sigma_{HI} = 1.0$ $M_\odot$ pc^{-2}.
[e] Values corrected for 0.21 mag of Galactic extinction. No corrections for internal extinction or inclination applied.
[f] Values from Paper I.
[g] Defined as $(M_{atomic} + M_{molecular})$/SFR, where $M_{atomic} \approx M_{molecular}$.
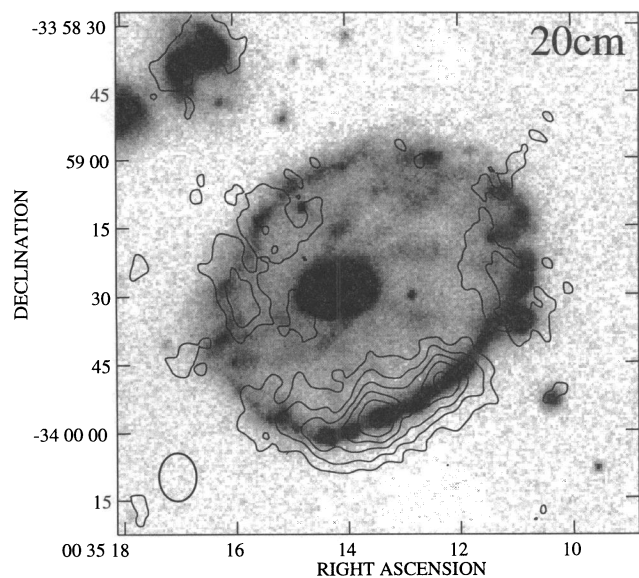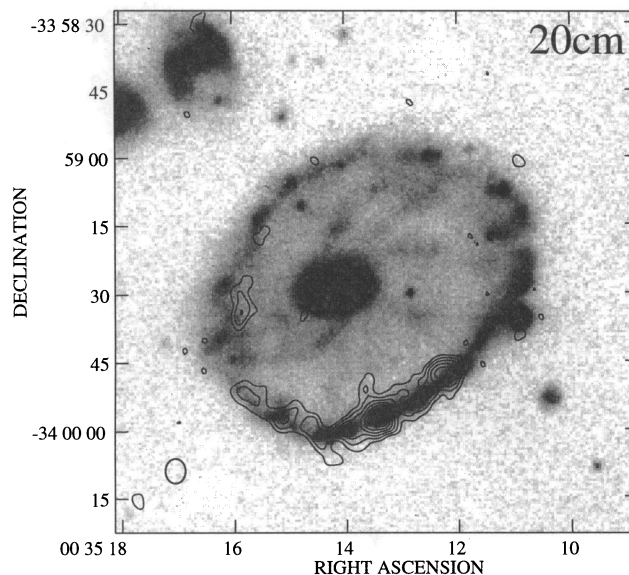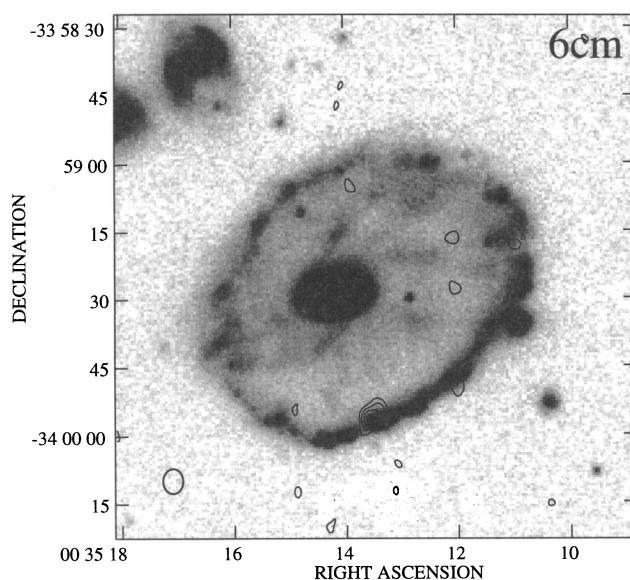
FIG. 4a

FIG. 4b

FIG. 4c

FIG. 4.—Radio continuum emission from the Cartwheel. (a) 20 cm (BCD), (b) 20 cm (BnA), (c) 6 cm (CnB). The contour levels are 3, 5, 7, 9, 11, 13, 15, and 17 times the 1 σ noise in each map (0.15, 0.14, and 0.07 mJy beam^{-1}, respectively). The radio contours are shown superposed on an R-band CCD image.

contained only H I emission that could be clearly associated with the ring galaxy, while the second received everything else in the system. These were used to construct "moment" maps of the integrated H I surface density, intensity-weighted velocity field, and line width in AIPS. Each map plane was first smoothed spatially with a Gaussian kernel to resolutions of 11″ (BCD) and 6″ (BnA) FWHM and Hanning smoothed to a velocity resolution of 42 km s^{-1}. Only pixels in the smoothed maps above the 2 σ noise level were used. Finally, a correction for primary beam attenuation was applied to the total intensity maps. The global distribution of 20 cm continuum and H I in the Cartwheel Group (BCD) is shown in Figures 3a and 3b, superposed on the CTIO 4 m prime focus image. A more detailed view of the radio continuum emission from the ring galaxy is presented in Figure 4, while Figures 5 and 6 show moment maps for the BCD and BnA "Cartwheel only" H I data sets,

respectively. The radio contours are shown superposed on an R-band CCD image in Figures 4, 5, and 6. Table 3 contains a compilation of each galaxy's integrated emission properties derived from these figures. Throughout this paper, neutral hydrogen surface density—Σ_{HI} ($M_\odot$ pc^{-2})—will be used rather than column density. Conversion between the two can be made using $N_{HI}/\Sigma_{HI} = 1.3 \times 10^{20}$ cm^{-2} ($M_\odot$ pc^{-2})$^{-1}$. Elsewhere, the symbols $\Sigma_{20\,cm}$, $\Sigma_{6\,cm}$, and $\Sigma_{H\alpha}$ will be used to denote 20 cm, 6 cm, and Hα surface brightness.

Average azimuthal and radial profiles for the ring galaxy were constructed using the continuum and "Cartwheel only" moment maps. The Cartwheel's disk was first decomposed into a series of elliptical annuli one-half to one-third synthesized beam in width. Since the Cartwheel has two rings with slightly different axis ratios, centers, and position angles, the annuli were constrained to match the inner and
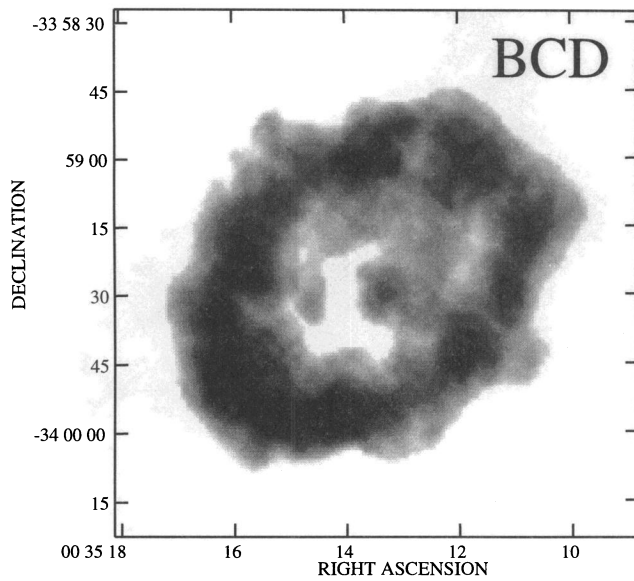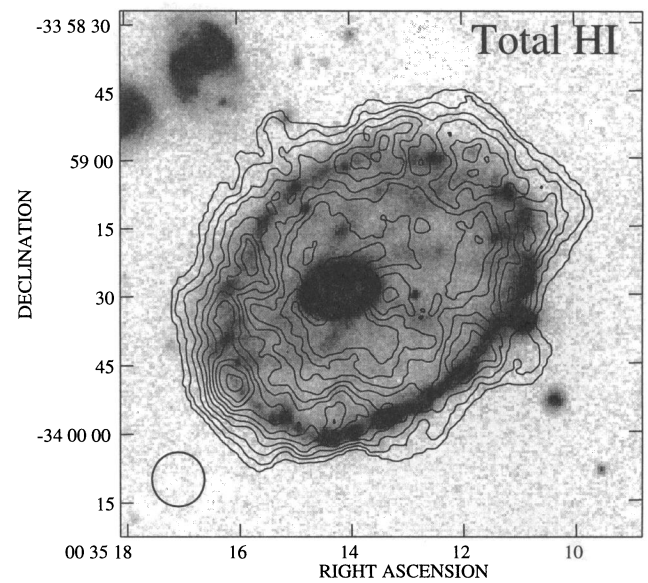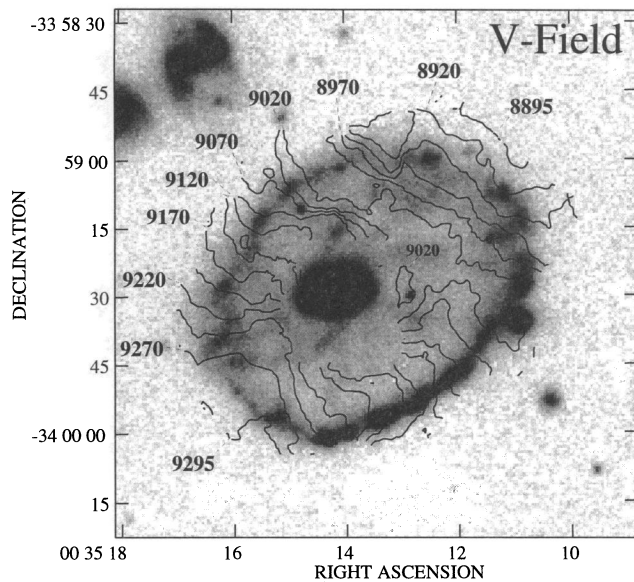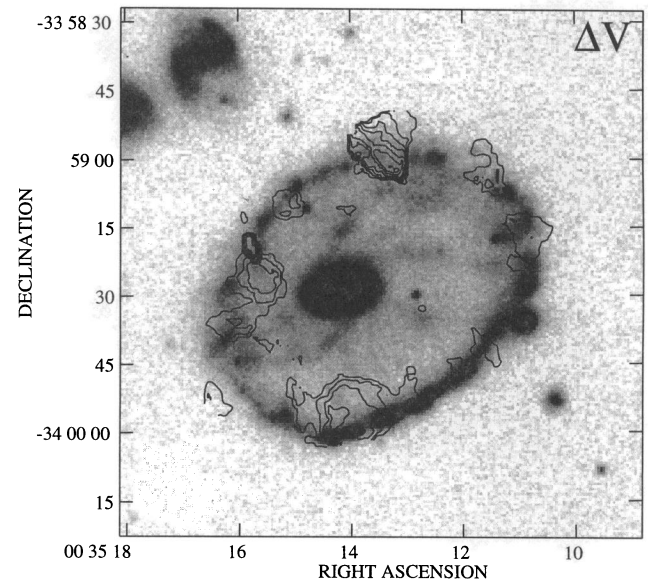
FIG. 5a

FIG. 5b

FIG. 5c

FIG. 5d

FIG. 5.—Neutral hydrogen moment maps of the Cartwheel using the BCD database: (a) Integrated H I shown in gray scale (linear stretch). (b) H I contours on an R-band CCD image. The levels correspond to 1, 4, 7, 10, 13, 16, 19, 22, 25, and 28 $M_\odot$ pc^{-2}. (c) Flux-weighted H I velocity field (km s^{-1}). (d) H I line widths. The contours are in increments of 5 km s^{-1}, starting at 40 km s^{-1}.

outer rings at their respective radii and to vary smoothly in between. The variations in Σ_{HI} and $\Sigma_{20\,cm}$ with position angle ϕ, measured counterclockwise from north of the outer ring's projected center, were derived by computing the mean and 1 σ uncertainty within 6° segments of an annulus centered on the outer ring. These are shown in Figure 7. Similarly, azimuthally averaged radial profiles were derived by computing the mean and 1 σ uncertainty within each annulus for a range of radii and are presented in Figure 8. Azimuthal and radial $\Sigma_{H\alpha}$ profiles from Paper I are included for comparison.

3. RESULTS

3.1. Radio Continuum Emission in the Cartwheel

Figure 3a shows that the ring galaxy dominates the 20 cm continuum emission of the Cartwheel Group, contributing 11.5 ± 0.2 mJy, or 85% of the group's total. Radio continuum is almost entirely confined to the Cartwheel's outer ring and is greatly enhanced in the ring southern quadrant ($\phi = 120°-250°$), the region experiencing peak MSF. Emission extending into the disk is seen in the southern quadrant's wake and in sections of the ring east and northeast of the nucleus ($\phi \approx 45°-90°$). The higher resolution BnA 20 cm map (Fig. 4b) shows a clear association between radio continuum emission and the giant H II complexes of the ring, with peaks coincident with the two most Hα luminous examples (CW 17 and 23; Paper I). The continuum sources 20″ east and northeast of the nucleus are clearly offset from the outer ring, and a finger of emission projects inward from a part of the ring near CW17. The loop of emission associated with the outer ring west of the Cartwheel's nucleus in Figure 4a is of marginal significance and may not be real, as no emission is seen in this part of the ring in the BnA map.
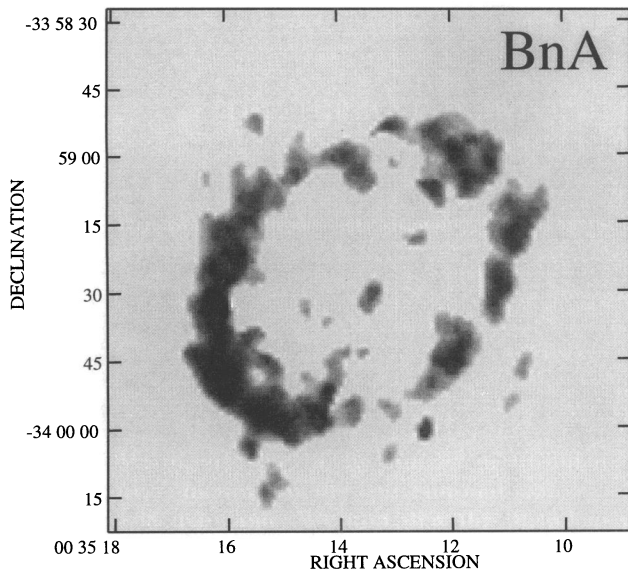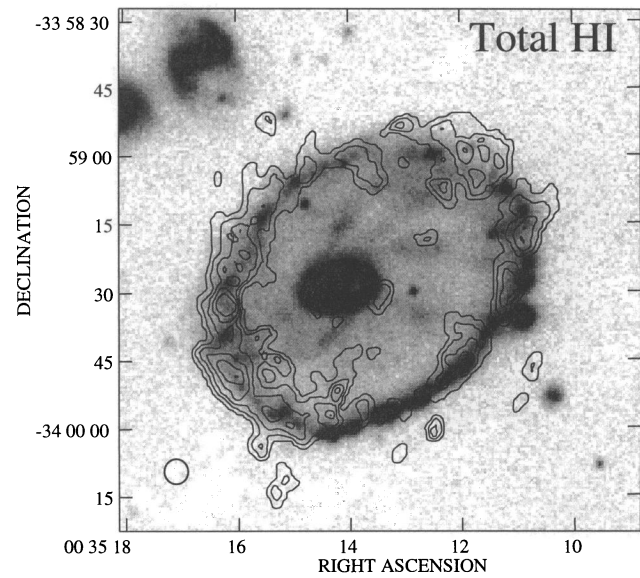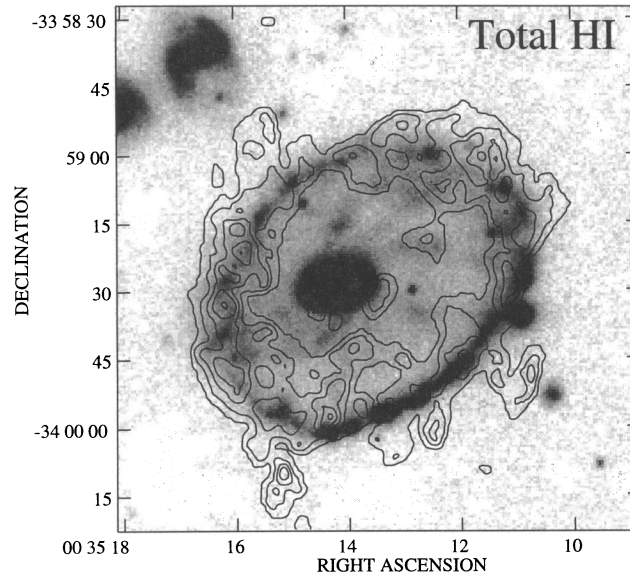
FIG. 6a

FIG. 6b

FIG. 6c

FIG. 6.—Neutral hydrogen moment maps of the Cartwheel using the BnA database: (a) Integrated H I shown in gray scale (linear stretch). (b) H I contours on an R-band CCD image. The levels correspond to 2, 12, 22, 32, 42, 52 $M_\odot$ pc^{-2}. (c) Same as (b), but with additional velocity smoothing and a lower threshold.

Figure 7b shows the azimuthal variations in $\Sigma_{20\,cm}$ around the outer ring derived from the BnA map, while Figure 7c shows $\Sigma_{H\alpha}$ versus ϕ at the same resolution. The two profiles are almost identical.

At 6 cm (Fig. 4c), only CW17 and 23 are detected, and a total flux of 2.3 ± 0.3 mJy is measured. Of the Cartwheel's H II region complexes, CW 17 possesses the highest 20 cm, 6 cm, and Hα luminosities. No significant continuum emission was detected from the Cartwheel's nucleus, inner ring, or optical spokes in either continuum data set.

3.2. H I in the Cartwheel

3.2.1. Spatial Distribution

A total H I mass of 1.6×10^{10} $M_\odot$ was measured in the Cartwheel Group using Figure 3b. This is 84% of the single-

dish value but within the uncertainty quoted by Mebold et al. (1977). The Cartwheel clearly possesses the bulk of the system's neutral gas. Using the BCD "Cartwheel only" total H I map (Fig. 5a), a $M_{H I}$ of 9.3×10^9 $M_\odot$ was derived for the ring galaxy, or ~60% of the group's total. Figure 5b shows that more than 85% of this (8.0×10^9 $M_\odot$) is organized into a clumpy distribution coinciding with the optical outer ring. The large-scale H I distribution of the ring is dominated by a systematic rise and fall in $\Sigma_{H I}$ over $\phi \sim 10°$–190°. This is not simply a projection effect, since a similar enhancement would have been expected on the opposite half of the ring. The H I distribution departs from an ellipse at low Σ_H in several locations along the ring. One occurs in the northwest ($\phi \sim 270°$–320°), where the $\Sigma_{H I}$ contours are noticeably boxlike below 3.5 $M_\odot$ pc^{-2}. At a number of other locations, gas is found projecting away
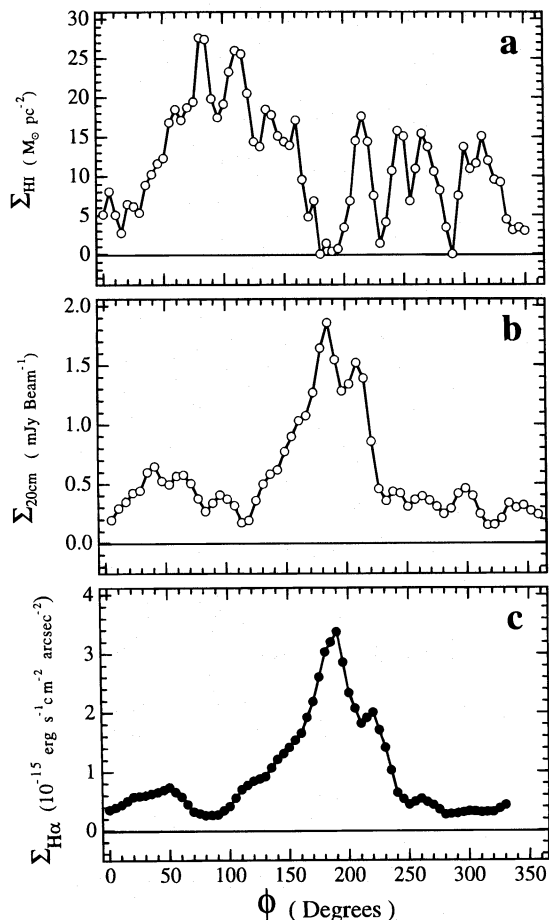
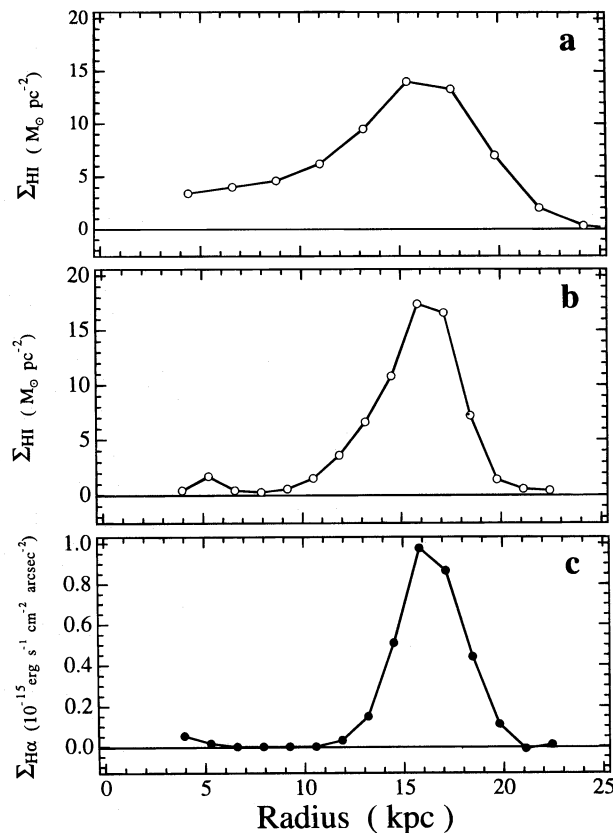FIG. 7.—Averaged azimuthal profiles around the Cartwheel's outer ring in (a) BnA Σ_{HI}, (b) BnA Σ_{20cm}, and (c) $\Sigma_{H\alpha}$.

FIG. 8.—Azimuthally averaged radial profiles for the Cartwheel in (a) BCD Σ_{HI}, (b) BnA Σ_{HI}, and (c) $\Sigma_{H\alpha}$.

from the ring, most notably in the northeast (e.g., $\phi = 35°$) and southern ($\phi = 190°-245°$) quadrants.

Faint optical emission fills the region between the inner and outer rings of the Cartwheel (Paper I; Marcum, Appleton, & Higdon 1992; FH). Figures 5a and 5b show that low surface density H I is also present. Over a region having the shape and orientation of the outer ring and a semimajor axis of 26″, a total M_{HI} of 1.3×10^9 $M_\odot$ and $\Sigma_{HI} = 4.5$ $M_\odot$ pc^{-2} was measured. Interesting structure can be seen in this component: An irregular H I "hole" exists where the Cartwheel's nucleus, bar, and much of the inner ring reside. No H I was detected here even after additional smoothing of the map cube, implying $\Sigma_{HI} < 0.3$ $M_\odot$ pc^{-2} (3 σ). A second extended region of depressed H I surface density is located 12″ inward and parallel to the ring at $\phi \sim 270°$ ($\Sigma_{HI} = 2.5$ $M_\odot$ pc^{-2}). Two broad H I streams extend through the disk and terminate near the inner ring's major axis. The first begins $\sim 20″$ north of the Cartwheel's nucleus and stretches in a counterclockwise arc to the inner ring. This feature then appears to cross the inner ring near its eastern major axis line of nodes before ending in a small concentration of H I near the southeastern end of the small nuclear bar. The other H I extension traces a nearly linear path from the southwestern portion of the outer ring ($\phi = 225°$) to the western major axis of the inner ring, where it projects onto an H I concentration just beyond the inner ring. Compared with its eastern counterpart, this clump is twice as massive (2×10^7 $M_\odot$) and possesses a higher peak Σ_{HI} (9.5 vs. 4.2 $M_\odot$ pc^{-2}). A significant mass of H I is accumulating near

the inner ring. However, no clear association is seen between H I in the disk and the Cartwheel's optical spokes. For example, half of the two prominent spokes connecting the eastern outer ring ($\phi = 100°$) with the southwestern portion of the inner ring reside in the central H I hole in Figure 5b. Moreover, the two H I streams do not coincide with any obvious optical features in the disk.

Figure 8a shows the mean radial Σ_{HI} profile, averaged over 360° in ϕ. The same average radial dependence seen in starlight—i.e., a steady increase in optical surface brightness with radius, followed by a sharp drop beyond the outer ring—is found in H I (Paper I; Marcum et al. 1992). A search for low Σ_{HI} disk beyond the outer ring was made by increasing the velocity smoothing in computing the total H I maps. No H I was detected beyond the outer ring above an 0.3 $M_\odot$ pc^{-2} upper limit (3 σ). FH suggested that the low metallicities observed in the Cartwheel H II regions were the result of the ring propagating into an extended disk of unprocessed gas. Such a disk does not exist, unless it possesses a very low Σ_{HI}. The simplest explanation is that the outer ring has reached the edge of the precollision H I disk or has just moved beyond it.

The distribution of Σ_{HI} at higher resolution is shown in Figures 6a and 6b. A total M_{HI} of 6.3×10^9 $M_\odot$ was derived, which is 75% of the ring's H I mass found using the BCD data. Figure 6b shows that this material is almost entirely restricted to the outer ring. The clumpiness of the ring H I distribution is emphasized, and extended emission (e.g., the disk H I component) has been resolved out. While larger values of Σ_{HI} are found (average and peak Σ_{HI} are 16.3 and 61.0 $M_\odot$ pc^{-2}), the overall distribution of H I in the ring is much the same. The average change in Σ_{HI} (BnA)

with ϕ around the outer ring is shown in Figure 7a: Σ_{HI} varies from ~ 0 to 28 $M_\odot$ pc^{-2}, with a mean value of 9.3 $M_\odot$ pc^{-2}. The corresponding averaged radial variations in Σ_{HI} are shown in Figure 8b. Neutral hydrogen is found interior to the outer ring, such as the two H I clumps near the inner ring in Figure 6b. H I is also found projecting inward from the outer ring in a number of locations. However, obvious H I counterparts of the spokes are still not apparent above a limiting Σ_{HI} of 0.8 $M_\odot$ pc^{-2}. A number of small but significant clumps of H I are found *beyond* the outer ring in the vicinity of the southern quadrant, the largest having M_{HI} and Σ_{HI} similar to the H I concentrations near the inner ring. A second version of the BnA H I map was made with increased velocity smoothing in an attempt to recover higher dispersion gas and is shown in Figure 6c. Little difference is seen between Figures 6a and 6c over most of the ring. However, a noticeably disturbed H I morphology becomes apparent in the southern quadrant. The H I clumps beyond the ring in Figure 6b form filaments associated with the most luminous ring star forming regions. A similar feature is seen northeast of the nucleus near the H II region complex CW 3. The total H I mass associated with these filament-like features is $\sim 7 \times 10^8$ $M_\odot$. The finger-like projections of H I south of the ring nucleus form a loop with the ring to the west in Figure 6c, and the trailing gas near $\phi \sim 220°$ extends further into the disk. Note that while additional smoothing revealed low Σ_{HI} associated with the outer ring, the Cartwheel's spokes remained undetected in H I.

3.2.2. Kinematics

The Cartwheel's intensity-weighted H I velocity field (BCD) is shown in Figure 5c. A clear gradient in radial velocity across the disk of the ring galaxy is evident in both figures, with larger values found in the southeast. The disk's orientation must be deduced indirectly, since the lack of a strong bulge component precludes the use of dust or large scale reddening signatures (see, e.g., de Vaucouleurs 1958). However, collisional ring galaxy models always generate trailing spokes. Together with the velocity field, this places the southern quadrant on the galaxy's far side. Noncircular gas motions are apparent in the noticeable twist in the kinematic line of nodes in the southwest half, and the kinks in the velocity contours across the outer ring. The lack of a clear "S" type distortion in the velocity field argues against a highly warped disk.

To analyze the ring galaxy's kinematics, the H I distribution in Figure 5a was decomposed into a series of elliptical annuli of width 3″5, each subdivided into 6° sectors in azimuth ψ (measured counterclockwise from the outer ring major axis line of nodes). The mean H I radial velocity (V_{rad}), 1 σ uncertainty, and Σ_{HI} were computed as a function of ψ at each radius. Velocity measurements were weighted according to the ratio of M_{HI} measured in that sector to that of the annulus, which de-emphasized regions where the radial velocity was less well determined. Position angle varied smoothly between the values derived at the inner ring's (102°), and outer ring's (129°) radii. Simple models were then fitted to radial velocity–position angle (V_{rad}-ψ) diagrams at each radius. This technique is well understood and has the advantage of making noncircular motions obvious (e.g., van der Kruit 1974; Buta 1986). The two rings should be nearly circular, since the centers of the two rings differ by only 7″ ($\sim 15\%$ of the Cartwheel's radius), which

indicates a small impact parameter. In fact, the sharply defined inner ring points to a symmetric perturbation even at this small radius, implying that the impact was within 5″ of the nucleus. Therefore, only models of circular, inclined, and rotating rings—with and without expansion—were considered. The expectation that the rings represent rotating and expanding structures (cf. Toomre 1977) is well supported by optical kinematic studies (FH; Few, Madore, & Arp 1982; Taylor & Atherton 1984; Jeske 1986), and only *expanding* rings can account for the observed radial color gradients (see, e.g., Marcum et al. 1992). The systemic (V_{sys}), rotational (V_{cir}), and expansion (V_{exp}) velocities were determined by minimizing the sums of the squares of the residuals between the model and observed radial velocities ($V_{rad,\psi}$) in each annulus of radius R,

$$\chi^2 = \sum_\psi w_\psi^2 [V_{rad,\psi} - V_{sys}$$
$$- (V_{cir} \sin i \cos \psi + V_{exp} \tan i \sin \psi) Q_\psi^{-1}]^2 , \quad (1)$$

where

$$Q_\psi = \sqrt{\sec^2 i - \tan^2 i \cos^2 \psi} . \quad (2)$$

In the above, i is the inclination, taken to be a constant 41° [$\cos^{-1}$ (minor axis/major axis) for the outer ring], and w_ψ is the weight assigned to each measurement. For nonexpanding rings, $V_{exp} = 0$ in equation (1). Formal uncertainties in V_{sys}, V_{cir}, and V_{exp} were derived using

$$\sigma^2(V_x) = \sum_\psi w_\psi \left(\frac{\partial V_x}{\partial V_\psi}\right)^2_{\psi'} \delta V^2 , \quad (3)$$

where $\partial V_\psi = V_{model} - V_{rad,\psi}$ at ring position angle ψ, δV is the velocity resolution (42 km s^{-1}), and where V_x denotes either V_{sys}, V_{cir}, or V_{exp}.

The V_{rad}-ψ diagram for the outer ring ($R = 16.9$ kpc) is shown in Figure 9, with the best fit rotating/expanding (*solid line*) and rotating (*dashed line*) circular ring models overplotted. The rotating/expanding ring model provides a significantly better fit to the data. The derived velocities and formal uncertainties are $V_{sys} = 9089 \pm 5$ km s^{-1}, $V_{cir} = 291 \pm 9$ km s^{-1}, and $V_{exp} = 53 \pm 9$ km s^{-1}. FH found $V_{cir} = 254$ km s^{-1} and $V_{exp} = 89$ km s^{-1} using a similar technique but with only five velocity measurements. An indicative mass (M_{ind}) of $(3.4 \pm 0.2) \times 10^{11}$ $M_\odot$ was estimated using the outer ring's radius and rotation speed, which is 30% higher than FH's determination.
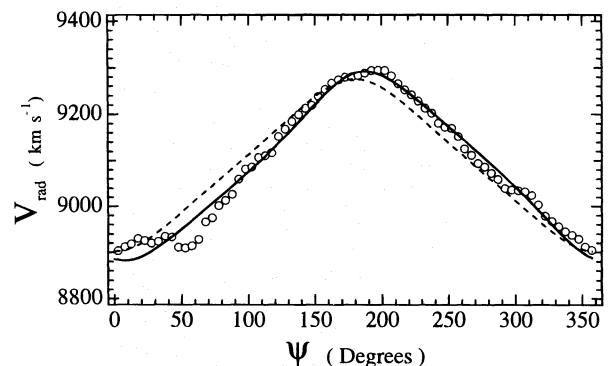

FIG. 9.—Radial velocity–position angle diagram for the Cartwheel's outer ring ($R = 16.9$ kpc) using the BCD velocity field of Fig. 5c. The solid line shows a least-squares fit to an inclined circular, rotating, and expanding ring model, while the dashed line corresponds to a rotating model. Using the former, $V_{sys} = 9089 \pm 5$ km s^{-1}, $V_{cir} = 291 \pm 9$ km s^{-1}, and $V_{exp} = 53 \pm 9$ km s^{-1} are derived.
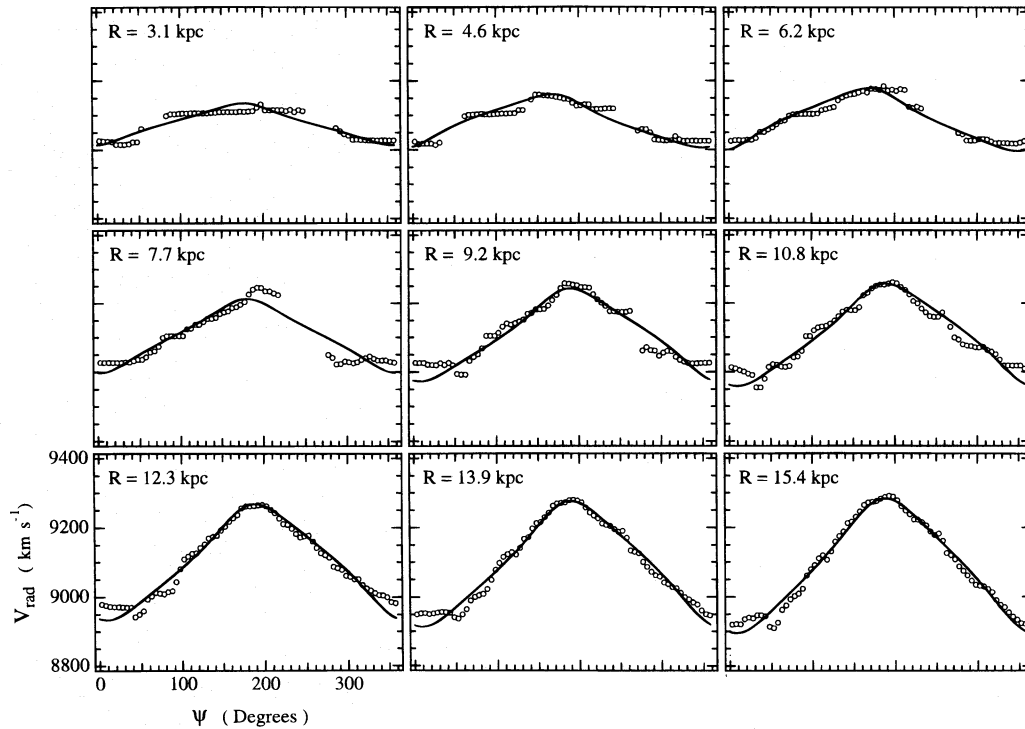
FIG. 10.—Radial velocity–position angle diagrams at intermediate radii. A least-squares fit to an inclined circular ring model with rotation and expansion is shown overplotted in each panel. The radius of each annulus is shown.

Figure 10 shows V_{radial}-ψ diagrams for H I in the Cartwheel at intermediate radii. Overplotted on each panel is the least-squares fit to a rotating/expanding inclined circular ring model. Gaps in the diagrams represent sectors in which no H I was found. This simple model fits the data well at all radii. Derived values of V_{cir} and V_{exp} versus radius are listed in Table 4 and are shown graphically in Figure 11. The Cartwheel's disk exhibits solid body rotation in the rotation curve of Figure 11a, while changes in V_{exp} in Figure 11b indicate (1) a general increase in V_{exp} with radius, which

TABLE 4
RESULTS OF VELOCITY FIELD ANALYSIS

R (kpc)	V_{sys} (km s^{-1})	V_{cir} (km s^{-1})	V_{exp} (km s^{-1})	Σ_{crit} ($M_\odot$ pc^{-2})
3.1......	9085.2 ($\pm$2.2)	76.6 ($\pm$0.2)	$-$8.6 ($\pm$6.6)	14.0
4.6......	9086.0 ($\pm$2.4)	94.8 ($\pm$4.8)	$-$30.9 ($\pm$7.6)	12.8
6.2......	9088.1 ($\pm$2.6)	114.7 ($\pm$5.6)	$-$33.4 ($\pm$6.2)	11.3
7.7......	9101.6 ($\pm$6.4)	143.1 ($\pm$11.0)	1.8 ($\pm$17.0)	11.1
9.2......	9108.9 ($\pm$7.0)	177.1 ($\pm$13.2)	41.3 ($\pm$4.4)	11.8
10.8......	9108.3 ($\pm$5.8)	198.6 ($\pm$12.2)	48.3 ($\pm$8.0)	11.8
12.3......	9101.0 ($\pm$4.8)	227.6 ($\pm$10.6)	50.0 ($\pm$6.6)	11.2
13.9......	9095.2 ($\pm$5.2)	250.2 ($\pm$11.4)	57.1 ($\pm$8.0)	11.3
15.4......	9090.1 ($\pm$4.8)	275.7 ($\pm$0.4)	51.0 ($\pm$8.6)	11.0
16.9......	9088.5 ($\pm$5.2)	291.2 ($\pm$9.2)	53.0 ($\pm$8.8)	10.5

becomes shallower close to the outer ring, and (2) negative V_{exp} for $R \lesssim 8$ kpc. These trends indicate that gas close to the outer ring is not expanding as fast as gas in the ring itself, as would be expected if material is beginning to return to smaller radii. The negative V_{exp} implies that gas is infalling near the inner ring, where H I concentrations are found. These results agree well with the models of SMH, which combined a smoothed particle hydrodynamic (SPH) algorithm (local self-gravity) with a preliminary version of the H I rotation curve.[5] SMH found that a massive halo was needed to reproduce both the observed kinematics and the relative sizes of the two rings. Inclusion of a halo resulted in uniformly expanding rings, which, given the outer ring's radius and V_{exp}, implies that 313 $\pm$ 48 Myr has elapsed since the intruder's passage.
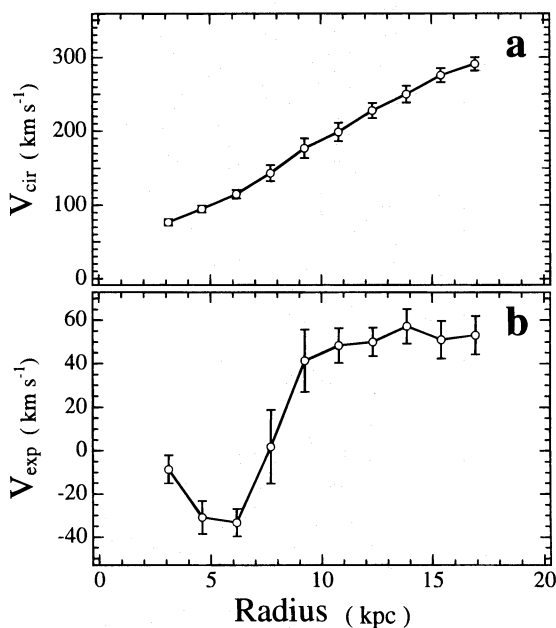

FIG. 11.—Derived (a) rotation curve and (b) variation in expansion velocity with radius from the model fits. The inner and outer rings are located at radii of 3.7 and 16.5 kpc, respectively.

[5] Because the annular regions of the Cartwheel's disk used to determine V_{exp} and V_{cir} were defined differently in SMH and this work, SMH's Fig. 6a ("Outer ring centered") corresponds to Fig. 11 for $R > 10$ kpc, while Fig. 6b ("Potential centered") should be compared with Fig. 11 for $R \lesssim 10$ kpc.

3.2.3. H I *Line Widths in the Ring Galaxy*

A map of the H I line width for the Cartwheel derived using the BCD data is shown in Figure 5d. Most of the gas, and essentially all of the low $\Sigma_{H I}$ disk bounded by the outer ring, possesses $\Delta V \lesssim 40$ km s^{-1}, which is the velocity resolution of the moment maps. Still, a few regions in which ΔV is significantly greater are found in the outer ring. Only three are clearly associated with sites of MSF as traced by Hα: the H II region complexes CW 3–5 ($\phi = 15°$–45°), the southern quadrant, and the H II region complexes CW 24–26 ($\phi = 270°$–320°). Of these, the largest line widths (~ 60 km s^{-1}) are associated with the extended region of gas *interior* to H II complexes CW 12–16 in the southern quadrant and not the more luminous CW 17. On the other hand, several luminous H II region complexes (e.g., CW 10 at $\phi = 147°$) are found in regions of low ΔV, and several regions of comparatively low MSF activity show fairly large line widths. One is located 20″ east of the Cartwheel's nucleus, while another is found on the ring at $\phi = 0°$. Finally, the H I blobs just beyond the inner ring possess $\Delta V \lesssim 40$ km s^{-1}.

3.3. *Radio Emission from the Companions*
3.3.1. *Radio Continuum*

Companions G1 and G3 have comparable 20 cm continuum fluxes (1.4 and 0.9 mJy, respectively). Figure 3a shows

that their 20 cm and optical morphologies agree well with one another, with radio emission enhanced near star-forming regions in both cases. An upper limit of 0.2 mJy (3 σ) was placed on 20 cm emission from the early-type galaxy G2. None of the companion galaxies was detected at 6 cm to an upper limit of 0.2 mJy (3 σ).

3.3.2. *Neutral Hydrogen*

Maps of the total H I surface density and flux-weighted velocity field for emission not obviously associated with the ring galaxy are shown in Figure 12. Companion G1 possesses 2.7×10^9 $M_\odot$ of H I, or roughly 30% of the Cartwheel's H I mass. The optical and H I distributions are similar for $\Sigma_{H I} > 10$ $M_\odot$ pc^{-2}. At lower levels, a more extensive H I envelope is found, though its overall shape is roughly that of G1's faint optical disk. The velocity field appears fairly typical for a differentially rotating disk galaxy. G1's kinematic and photometric axes differ by $\sim 15°$, indicating a recent interaction. Companion G2 was not detected in H I, which is not surprising given its lack of optical line emission and red color (Davies & Morton 1982; FH). From the 1 σ noise levels in the channel maps and the galaxy's optical velocity dispersion (300 km s^{-1}; Davies & Morton 1982), $M_{H I} < 8 \times 10^6$ $M_\odot$ (3 σ). Companion galaxy G3 possesses 6.5×10^8 $M_\odot$ of H I, or $\sim 7\%$ of the Cartwheel's $M_{H I}$. Its H I distribution is clearly distorted: The H I peak does not correspond with the optical center of
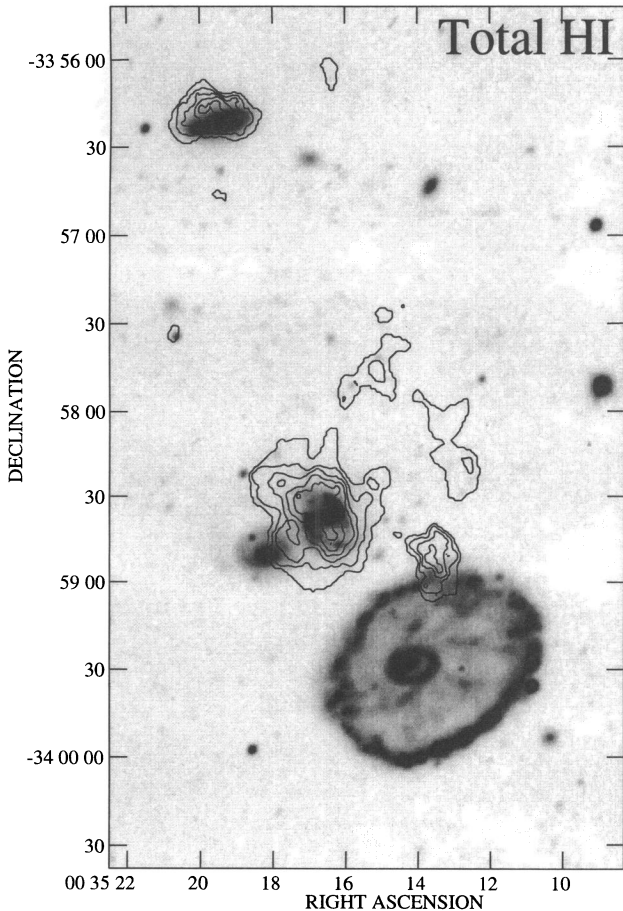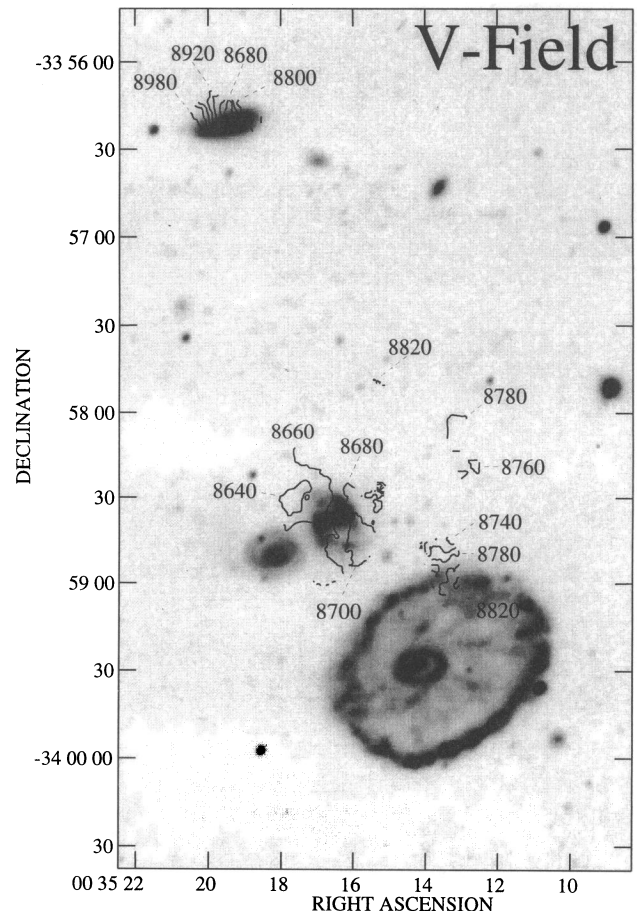

Fig. 12a

Fig. 12b

FIG. 12.—BCD moment maps using emission from the companion galaxies and field: (a) Integrated H I. The contours levels correspond to 1, 4, 7, 10, 13, 16, 19, 22, 25, and 28 $M_\odot$ pc^{-2}. (b) The flux-weighted H I velocity field.

the disk, and a diffuse low Σ_{HI} component is seen extending to the north. The peculiar H I distribution is not the result of an error in the optical-radio overlay, since $\Sigma_{20\ cm}$ agrees well with G3's optical structure (Fig. 3a). Despite these peculiarities, the flux-weighted H I velocity field of G3 shown in Figure 12b appears regular.

Faint H I emission not clearly associated with any group member is apparent in the moment maps (Figs. 3 and 12). This gas possesses mean and peak Σ_{HI} of 2.2 and 5.0 $M_\odot$ pc^{-2}, with the largest Σ_{HI} found just north of the Cartwheel's outer ring at $\phi = 0°$ (near CW 1). This latter H I cloud shows velocities significantly lower than the surrounding ring H I and is associated with large ΔV (Fig. 5d) and highly twisted velocity contours in the ring. Both 20 cm and Hα maps show this region to be relatively quiescent in terms of MSF, so it is doubtful that this H I represents material blown out of the galaxy. A more likely origin is infalling H I debris left in the intruder's wake. The elongated shape of this emission suggests tidal stretching, which might be expected of an infalling gas cloud.

Extensive low Σ_{HI} can be seen in the channel map centered at 8808 km s^{-1}. Here a large plume of gas is found projecting from the Cartwheel's center toward companion G3. The H I mass of this structure is $2 \times 10^9\ M_\odot$, or nearly 20% of the ring galaxy's. A large fraction of this gas exists in the single-velocity channel, which, together with its low surface density ($\Sigma_{HI} = 0.8\ M_\odot$ pc^{-2}), accounts for its failure to show up prominently in the total H I maps.

The BCD channel maps were used to compute effective single-dish H I spectra of G1 and G3. Estimates of the companion's indicative masses were then made using

$$\left(\frac{M_{ind}}{10^9\ M_\odot}\right) = 3 \times 10^{-5}\left(\frac{D}{kpc}\right)\left(\frac{\Delta V_{20\%}}{\sin i}\right)^2 \qquad (4)$$

(Balkowski 1973), which gave values of 1.4 and 1.0×10^{10} $M_\odot$, for G1 and G3. Using an empirical velocity dispersion–mass relation, Davies & Morton (1982) estimated G2's $M_{ind} \sim 2 \times 10^{10}\ M_\odot$. Neither companion appears to possess an M_{ind} greater than 6% of the Cartwheel's disk + halo. Note that G2's closed isovelocity contours in Figure 12b indicate a falling rotation curve, and thus no massive halo.

4. DISCUSSION

4.1. Radio Continuum Properties of the Outer Ring
4.1.1. Radio Spectral Indices and Extinction

Radio spectral indices ($S \sim v^\alpha$) of the two H II region complexes were determined using the 6 cm and 20 cm continuum flux within identical 10″ diameter apertures. The resulting values were $\alpha = -0.6 \pm 0.2$ (CW 17) and -0.7 ± 0.3 (CW 23), which indicates a strong nonthermal component as expected from the large numbers of massive stars. The exponents resemble those seen in other giant extragalactic H II regions (Kaufman et al. 1987; van der Hulst et al. 1988).

While the 6 cm measurements contain a significant nonthermal contribution, useful upper limits to A_V can be derived when combined with the Hα flux within identical 10″ diameter apertures. Using $T_e = 14,000$ K (FH), a standard Galactic reddening law (Miller & Mathews 1972), and computed ratios of Hα to thermal free-free emission (Gebel 1968), visual extinctions (A_V) of 1.6 ± 0.2 (CW 17) and 2.1 ± 0.3 (CW 23) were derived. Both values are in reason-

able agreement with $A_V = 2.1$ (FH) using Balmer line ratios and are somewhat greater than A_V derived this way in other extragalactic H II regions (e.g., $\bar{A}_V = 1.1 \pm 0.4$ for 42 H II regions in M81; Kaufman et al. 1987).

4.1.2. The Relationship between 20 cm and MSF

Continuum emission at 20 cm in starburst regions is believed to arise from supernova remnants and can be used to trace recent MSF (Condon & Yin 1990). The close similarity between azimuthal variations in $\Sigma_{20\ cm}$ and $\Sigma_{H\alpha}$ (Figs. 7b and 7c) in the ring shows that Hα reliably maps the distribution of MSF in this galaxy. In particular, the observed crescent of Hα in Paper I, expected from a small impact parameter intruder passage, is not an artifact of obscuration.

Eighty percent of the Cartwheel's Hα emission is concentrated in the southern quadrant ($\phi = 120°-250°$). Assuming a constant $A_{H\alpha}$ of 1.6 mag throughout, $L_{H\alpha}$ equals 6×10^{42} ergs s^{-1} at the adopted distance of 91 Mpc. Over this region, the SFR for massive ($M/M_\odot > 10$) stars is 8 $M_\odot$ yr^{-1} (Kennicutt 1983), i.e., one expects to form 0.1–1.0 OB star per year on average. Assuming that MSF has been fairly constant over the past ~ 20 Myr, one would also expect a Type II supernova rate (μ_{SN}) of 0.1–1.0 yr^{-1}. By comparison, μ_{SN} among noninteracting galaxies peaks at 0.01 yr^{-1} in Sc spirals (Caswell 1970). Using the relation between nonthermal radio emission and μ_{SN} derived by Condon & Yin (1990) using data from the Galaxy

$$\left(\frac{\mu_{SN}}{yr^{-1}}\right) = 9.2 \times 10^{-7}\left(\frac{D}{Mpc}\right)^2\left(\frac{v}{GHz}\right)^{-\alpha}\left(\frac{S_v}{mJy}\right), \qquad (5)$$

the southern quadrant's integrated $S_{1378\ MHz}$ gives a μ_{SN} of 0.1 ± 0.02 yr^{-1}, which agrees with the lower bound of the optical estimate.

4.2. The Relationship between H I and MSF
4.2.1. The Relative Spatial Distribution

Large and systematic differences in the distributions of neutral gas and massive stars are evident in Figures 4 and 5. Regions of high Σ_{HI} are invariably regions of relatively low $\Sigma_{H\alpha}$, and vice versa (e.g., the region of peak Σ_{HI} at $\phi = 130°$). A pronounced anticorrelation between $\Sigma_{H\alpha}$ and Σ_{HI} is seen throughout the southern quadrant in the azimuthal profiles of Figure 7, with Σ_{HI} reaching a minimum precisely where $\Sigma_{H\alpha}$ peaks. The total mass of ionized gas in the southern quadrant was estimated to be $\lesssim 2.5 \times 10^8\ M_\odot$, using the H$\alpha$ map of Paper I, and the mean electron temperature (14,000 K) and density ($\leq 10^2$ cm^{-3}) from FH. Since the H I mass in the same region is $\sim 1.5 \times 10^9\ M_\odot$, the H I deficit cannot be filled by ionized gas, nor is it likely that molecular gas contributes significantly. The minimum gas surface density required for the survival of molecular clouds is a function of metallicity (Franco & Cox 1986) and is at least 40 $M_\odot$ pc^{-2} in the $Z < 0.1\ Z_\odot$ Cartwheel. Given the extreme ambient UV radiation field and low Σ_{HI} ($< 9\ M_\odot$ pc^{-2}) in this region, the ISM will be primarily atomic. The total L_B of the southern quadrant was estimated to be $4.4 \times 10^9\ L_\odot$ using the B-band CCD image. Assuming a mean A_B of 2.6 (FH) and a M/L_B of 1, appropriate for blue irregular galaxies, $M_{stars} \sim 5 \times 10^{10}\ M_\odot$. The outer ring's mass appears to be dominated by young stars throughout the starburst southern quadrant, and the strong depression in Σ_{HI} over the southern quadrant can be most simply

explained as the *consumption* of the gas supply by the starburst.

On smaller scales, H II complexes are never found coincident with the H I peaks in the ring but, rather, adjacent to them (e.g., CW 3, 17, and 28). Figure 6b also shows that prominent H II complexes tend to be found slightly *beyond* the H I ring throughout the southern quadrant. This effect is most prominent for CW 12–15 and 24. The magnitude of this offset is as large as 4″ (1.7 kpc in projection) for CW 12–15 and CW 26 and 27. Near the very luminous CW 17, the apparent displacement is smaller. This effect is not believed to be the result of a misalignment in the radio and optical maps, since good agreement between the optical and H I rings is seen elsewhere in the galaxy. Shifting the maps to bring H I and Hα in the southern quadrant into coincidence results in an offset in other parts of the outer ring. The presence of H II complexes in advance of the H I ring is consistent with MSF occurring preferentially on the leading edge of a gaseous ring density wave. Additional evidence comes from the detection of secondary H II region complexes only *in advance* of the ring (Paper I).

4.2.2. Is There a Gas Threshold Effect?

It has been noted that MSF tends to occur in regions in which Σ_{HI} exceeds ~ 7 $M_\odot$ pc^{-2} (see Davies, Elliot, & Meaburn 1976; van der Hulst et al. 1987). Kennicutt (1989) compared the azimuthally averaged radial distributions of Hα, H I, and ^{12}CO ($J = 1$–0) in a sample of spirals and found a wide range in the minimum total gas surface density ($\Sigma_g = \Sigma_{HI} + \Sigma_{HeI} + \Sigma_{H2}$), where star formation "turned on" in the disk. Applying a simple gravitational stability criterion (Safronov 1960; Toomre 1964), the observed threshold behavior was reproduced with remarkable success: on large scales, star formation appears to depend only on the local values of Σ_g and a critical surface density, defined as

$$\Sigma_{crit} = \left(\frac{\sigma\beta}{3.36\ G}\right)\kappa\ , \qquad (6)$$

where σ is the velocity dispersion and κ is the epicyclic frequency. The quantity β is a factor of order unity that accounts for deviations from an ideal thin disk. Since κ is a function of radius, Σ_{crit} is also and typically declines slowly. When $\Sigma_g/\Sigma_{crit} < 1$, MSF is suppressed, but when this ratio equals or exceeds unity, robust MSF occurs. A gas threshold effect in the Cartwheel is suggested by the fact that Σ_{HI} over most of its interior is below that found in the disks of the so-called giant red spirals, which are gas-rich galaxies whose low Σ_{HI} disks experience very low rates of MSF (van der Hulst 1987). This possibility was investigated by first computing $\Sigma(R)_{crit}$ using the H I rotation curve in Figure 11a. Values of σ (6 km^{-1}), and β (0.7) were adopted from Kennicutt (1989). Figure 13a shows the averaged BCD radial atomic gas Σ_{ag} ($= \Sigma_{HI} + \Sigma_{HeI} \approx 1.4 \times \Sigma_{HI}$; Brinks 1990) and Hα profiles for the Cartwheel, averaged over the entire disk. $\Sigma(R)_{crit}$ is shown as a dashed line. The atomic gas surface density exceeds Σ_{crit} only in the outer ring. Over the remainder of the Cartwheel, $\Sigma_{ag}/\Sigma_{crit} < 0.5$. Only in the outer ring of the Cartwheel does the measured atomic gas surface density exceed Σ_{crit}. The higher resolution data (Fig. 13b) show that $\Sigma_{ag}/\Sigma_{crit} \sim 3$ *on average* here. If $\Sigma_{ag}/\Sigma_{crit} \geq 1$ is a necessary condition for star formation, these results can account for the strong MSF in the outer ring and its
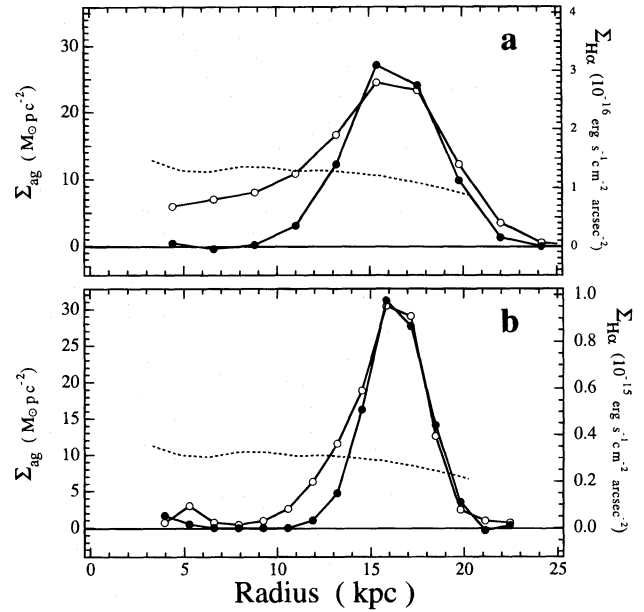

FIG. 13.—Comparison between radial surface brightness profiles of atomic (*open circles*) and ionized (*filled circles*) gas: (a) BCD Σ_{ag} and $\Sigma_{H\alpha}$ vs. radius, (b) BnA Σ_{ag} and $\Sigma_{H\alpha}$ vs. radius. The dashed line shows the radial variation in the critical surface density (Σ_{crit}) as described in the text.

absence throughout the Cartwheel's disk, spokes, inner ring, and nucleus.[6]

An obvious uncertainty is the contribution to Σ_g from H$_2$, which is expected to be a minor component due to the low metallicity and high ambient UV field. A rough estimate of M_{H2} in the Cartwheel was made using the empirical L_{FIR}-M_{H2} relation of Young et al. (1989). The Cartwheel's L_{FIR} (1.0×10^{10} $L_\odot$; Jeske 1986), implies $M_{H2} = (3 \pm 2) \times 10^9$ $M_\odot$, and that $M_{H2}/M_{HI} = 0.5$–0.1. Assuming the atomic and molecular gas distributions are similar, $\Sigma_{H2} \approx 1.4$ $M_\odot$ pc^{-2} in the disk, still not enough to reach Σ_{crit}. Other factors may contribute to increase Σ_{crit} and further retard MSF in the Cartwheel's disk. For example, the gas velocity dispersion may exceed 6 km s^{-1} but be less than the H I velocity resolution. One such extended region with $\Delta V > 40$ km s^{-1} is found interior to the southern quadrant.

This analysis can be applied to the outer ring as a whole. Figure 14 shows the BnA Σ_{ag} azimuthal profile versus $\Sigma_{H\alpha}$. The dashed line represents the value of Σ_{crit} at the ring's radius (11 $M_\odot$ pc^{-2}). There is enough atomic gas to bring essentially all of the outer ring above Σ_{crit}. Beyond this observation, the situation is more complicated: regions of the ring experiencing the highest rates of MSF are found where Σ_{ag} is nearly zero, and regions of the ring where Σ_{ag} is farthest above Σ_{crit} are characterized by low levels of MSF. While a gas threshold can account for the lack of strong MSF on large scales, it appears that other factors regulate star formation on $\sim$kiloparsec scales in the ring itself.

Kennicutt's (1989) analysis found that when $\Sigma_g/\Sigma_{crit} > 1$, MSF obeyed a Schmidt law with Σ_g of the form

$$\Sigma_{MSF} = a\Sigma_g^N \qquad (7)$$

with $N \approx 1.5$. To determine if MSF follows such a dependence with Σ_{HI} in the Cartwheel's outer ring, points in Figure 14 where $\Sigma_{ag}/\Sigma_{crit} > 1$ were plotted against the cor-

---

[6] Alternately, the low Σ_{ag} regions may not provide adequate shielding from UV photons, preventing the formation of molecular clouds required for MSF.
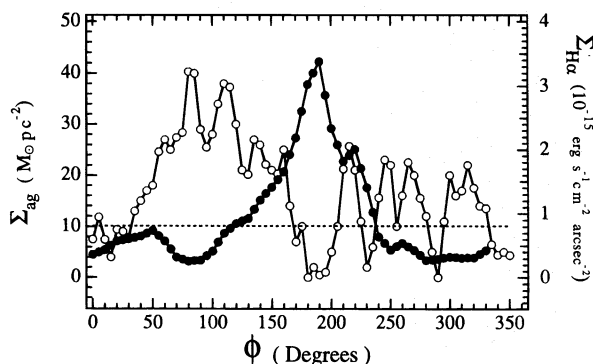
FIG. 14.—Averaged azimuthal variations in atomic (*open circles*) and ionized (*filled circles*) gas surface brightnesses around the outer ring using the BnA data. The dashed line shows the critical surface density (Σ_{crit}) at the outer ring's radius.

responding $\Sigma_{H\alpha}$ in Figure 15. The least-squares fit for data points outside the starburst southern quadrant (*open circles*) found an essentially zero slope ($N = 0.02 \pm 0.07$). A power-law relation was found for points from the southern quadrant (*filled circles*); however, the exponent was negative ($N = -0.58 \pm 0.24$), reflecting the anticorrelation between atomic gas and MSF. The exponent expected for classic Schmidt law behavior ($N = 1.5$) is not found.

Schmidt law behavior could be reconciled by an outer ring dominated by molecular gas. Analysis of Figure 7 in Kennicutt (1989) over the regime where a Schmidt law holds yields the following relation between H I, Hα, and H$_2$ surface densities:

$$\log \Sigma_{H\alpha} = 30.6 + 1.5 \log (\Sigma_{H I} + \Sigma_{H_2}) . \qquad (8)$$

Knowing $\Sigma_{H\alpha}$ and $\Sigma_{H I}$ allows a rough determination of Σ_{H_2} required for Schmidt law behavior throughout the Cartwheel's outer ring. Large molecular hydrogen surface densities are implied, with Σ_{H_2} ranging from 50 to 120 $M_\odot$ pc^{-2} in the southern quadrant. Such Σ_{H_2} could be detected through ^{12}CO ($J = 1-0$) emission in principle. For example, with $\bar{\Sigma}_{H_2} \sim 75$ $M_\odot$ pc^{-2} restricted to a 6″ wide ring, a 1′ FWHM single-dish beam would measure an $\bar{N}_{H_2} \sim 7.5 \times 10^{20}$ cm^{-2}. Assuming an $N(H_2)$–$I(CO)$ conversion determined in Galactic molecular clouds, this column density would produce peak antenna temperatures near 15 mK (Bloemen et al. 1986). Use of a conversion factor derived from observations of the lower metallicity LMC, perhaps more appropriate given the low oxygen abundances of the Cartwheel's ring, would give peak antenna temperatures of
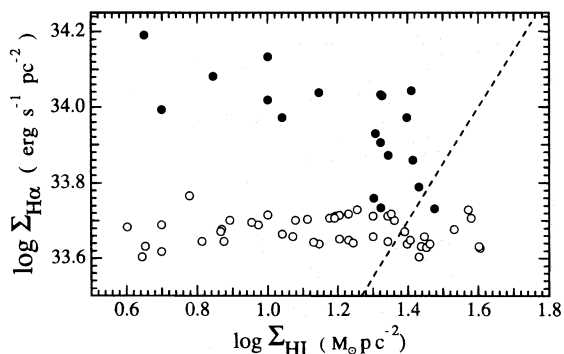
~ 3 mK. Recent observations by Horellou (1995) and Higdon, Lord, & Rand (1996) have reached sensitivities of 1 mK, which appears to rule out a large molecular component even for a low metallicity conversion factor. Deeper observations are needed to be certain. Alternately, spectroscopy or interference filter imaging in the 2.122 μm H$_2$ line could help constrain the molecular mass of the ring.

4.2.3. *MSF Triggering in The Ring*

Olson & Kwan (1990) concluded on the basis of their hydrodynamic models that high-speed disruptive cloud collisions ($V_{relative} \gtrsim 100$ km s^{-1}) were primarily responsible for starburst activity in interacting/merging galaxies. Such a process was thought to be at work in the Cartwheel's ring, with systematic variations in collision speeds around the ring arising from the slightly off-centered intruder passage, which resulted in the observed crescent of MSF (Paper I). However, the narrow H I line widths (Fig. 5d) and the absence of strong shear (Fig. 11a) show that strong shocks are not present in the ring, ruling out Olson & Kwan's mechanism in this system. Instead, the ring appears to initiate starburst activity primarily through concentration of the ISM in the ring. The lack of prominent H II complexes interior to the optical ring shows that stars more massive than B3 must not be common there, meaning that stars born in the narrow ring must spend at least 40 Myr in it. Because of dissipation, gas must spend *at least* as long in the ring. Note that $\gtrsim 40$ Myr ring confinement timescale is larger than the 30 Myr interval between peak ISM compression and robust MSF determined by Vogel, Kulkarni, & Scoville (1988) in M51. The combination of long confinement time, high densities, and lack of shocks makes the outer ring an ideal environment for the formation of very massive cloud complexes through coalescence. If the yield of massive stars is a function of the cloud mass, this provides a mechanism for the formation of large populations of OB stars and giant H II complexes. Scalo & Struck-Marcell (1986) found that a simple Oort model of the ISM displayed burst behavior when the average time between cloud collisions was smaller than the cloud lifetime. Above a critical value, SFR was found to be a strong function of cloud mass. Since the Cartwheel's ring is clearly a high-density environment and is likely characterized by high collision rates, this is an attractive mechanism to explain the ring burst. Systematic changes in the collision rate and speeds of clouds around the ring and stellar feedback may still influence the local SFR, giving rise to the observed Hα morphology.

4.2.4. *The Gas Consumption Timescale and Future MSF*

How long will the ring's gas supply last given the current SFR? Assuming comparable masses in the atomic and molecular gas components, $M_g \sim 2 \times 10^{10}$ $M_\odot$. If stars continue to form at the current rate, $\sim 25\%$ of this mass will be converted into stars (assuming $\epsilon_{SF} = 25\%$) by the time the ring has doubled in radius after 300 Myr. This indicates a rapid ISM consumption rate. Similarly defined gas depletion timescales in late spirals are on the order of several Gyr (Kennicutt 1983). The existence of large-scale color gradients in the outer ring's wake argue for a sustained starburst over the past 300 Myr. How much longer the ISM will continue to be concentrated in the orbit crowded outer ring and how much longer these high SFR will be supported is uncertain. If the ring starburst continues for another 300 Myr, there may be little gas left to fuel MSF in the inner ring, and what remains could be converted into stars in a

FIG. 15.—$\Sigma_{H\alpha}$ vs. $\Sigma_{H I}$ in the Cartwheel's outer ring where $\Sigma_{ag}/\Sigma_{crit} \geq 1$. Filled circles represent data from the starburst quadrant ($\phi = 120°$–$250°$). The dashed line shows the slope expected for a "classical" Schmidt law relation, with power-law exponent $N = 1.5$.

second ring-triggered starburst. The precollision Cart-wheel's ISM may be exhausted within ~0.6 Gyr of the intruder's passage.

4.3. *Gas in The Cartwheel's Inner Ring*

Higher order rings are a natural consequence of small impact parameter collisions and are also capable of trigger-ing separate propagating starbursts. The Cartwheel, Vela, and Arp 10 are the only known ring galaxies with inner rings (Taylor & Atherton 1984; Charmandaris, Appleton, & Marston 1993). Of the three, only the Cartwheel's shows no evidence of significant MSF, most likely because of a gas deficiency. But while the inner ring is *currently* H I poor, the Cartwheel's velocity field indicates that gas is beginning to return to smaller radii (Fig. 11b). If robust MSF will be prevented so long as $\Sigma_g/\Sigma_{crit} < 1$, an estimate of the amount of gas required to reach this threshold can be derived. Assuming a circular inner ring of radius 3.3 kpc and width of 1.8 kpc, a total gas mass of ~8×10^8 $M_\odot$ is needed to reach a uniform $\Sigma_{crit} = 11$ $M_\odot$ pc^{-2}, or more than 3×10^8 $M_\odot$ of H I, assuming equal masses of molecular and atomic gas. The values of Σ_{HI} and R in Table 3 where V_{exp} are negative can be used to estimate the time required for a given gas mass to reach the inner ring. Assuming the infall velocities remain fairly constant, ~1.4×10^8 $M_\odot$ of atomic gas will accumulate at the inner ring after 100 Myr. Unless this mass is distributed very nonuniformly, gas in the inner ring will be more than a factor of 2 below threshold. MSF will be retarded in the inner ring for at least the next ~100 Myr if the influx of gas does not significantly increase. This timescale increases if there is no significant molecular gas component.

Figures 5 and 6 show that H I is not totally absent from the inner ring. Gas has accumulated into at least one con-centration just *outside* the ring to the west and seems to coincide with the optical ring to the east. Optical maps of the inner ring show a "nick" in the light distribution across the ring in the west and a more extended spiral-shaped feature cutting through the ring to the northeast. Both are particularly noticeable in an unsharp-masked R-band CCD image of the inner ring and nucleus shown in Figure 16a. Both the western "nick" and its eastern counterpart are the result of dust lanes, as can be seen in a $V - R$ color index map of this field in Figure 16b. While there is evidence for dust throughout the region bounded by the inner ring, dust appears to flow primarily in a spiral-shaped stream from the inner ring to a small bar before reaching the nucleus. Figure 16c and 16d show the same optical map along with con-tours of Σ_{HI} (BCD and BnA). Clumps of H I are associated with the inner ring's nicks. The clear implication is that the densest H I concentration supplies the western dust lane and that gas is able to *cross* the inner ring to the east. It is tempting to speculate that the transfer of material across the ring will further contribute to the lack of MSF in this structure by siphoning off gas and preventing the build-up of high Σ_{HI}.

4.4. *Comparisons with Ring Galaxy Models*

As mentioned earlier, the Cartwheel's H I kinematics are well reproduced by the SPH + local self-gravity simula-tions of SMH. Spokelike features are formed in the disk, but they are not particularly gas rich. However, the outer ring does not contain the observed large fraction of the galaxy's gas content. Hernquist & Weil (1993, hereafter HW93) used a hybrid N-body/SPH algorithm to study the evolution of the stellar and gaseous components of the Cartwheel, with an eye toward understanding the nature of the spokes. Gaseous features resembling spokes form through fragmen-tation of the initially gas-rich outer ring, which becomes unstable because of dissipation and self-gravity. These frag-ments shear as they fall toward the disk's center. The devel-opment of stellar spokes is enhanced by the presence of the gas spokes. The model spokes are gas rich to the point of exceeding the outer ring's Σ_g. Even more ambitious were the attempts by Mihos & Hernquist (1994, hereafter MH94) combining a Schmidt law (SFR ~ $\rho^{1.5}$), an isothermal equa-tion of state, and energy feedback with an N-body/SPH code to simulate star formation in the Cartwheel. A gas-rich ring forms, parts of which fragment and return to the disk's center. As in HW93, this infalling gas is sheared into spoke-like structures, whose Σ_g and SFR soon exceed the outer ring's. MH94 conclude that Cartwheel-like ring galaxies have two phases of MSF: early on, the outer ring possesses most of the gas and essentially all the MSF. After the ring has fragmented, the spokes and inner ring possess the great-est gas densities and compression, and *they* dominate MSF. This backdrop of disk star formation complicates the inter-pretation of the radial color gradients found in ring galaxies (see, e.g., Marcum et al. 1992). However, the available evi-dence does not support the most important predictions of HW93 and MH94. First, this work has shown that the Cartwheel's spokes are not rich in neutral gas, and even at late stages of its evolution (i.e., after the inner ring has formed), the outer ring is the main reservoir of gas in the galaxy. Gas is flowing into the Cartwheel's inner disk but not along the spokes. Further, emission-line maps of the Cartwheel (Paper I) show that its inner ring and spokes are undetected in Hα and are at best much weaker than the outer ring in terms of MSF. Hα maps of other evolved ring galaxies (see, e.g., Higdon & Wallin 1996; Marston & Appleton 1995) show MSF to be *always* dominated by the outer rings and not the disk or inner ring. The analysis of radial color gradients therefore will not be significantly con-fused by ongoing star formation. On the plus side, by adding an extensive low-density gas disk (Σ_g ~ constant), MH94 did make high-Σ_g rings resembling those seen in Figures 5 and 6. Neither SMH or HW93 were able to produce models with the observed contrast between ring and disk Σ_{HI} without unreasonably massive intruders.

Apart from a lack of gas, other effects could retard MSF in the spokes, such as strong shear and elevated gas tem-peratures from past episodes of MSF. For example, the spokes may be the sheared remains of giant star-forming regions from the ring that have largely consumed, dispersed, or heated their gas content past the point at which signifi-cant MSF is possible. This underscores the need for more realistic treatments of the starburst ISM, including heating and cooling terms, the effects of shear, and multiple phases. Finally, it is worrisome that spokes should be so easily formed in ring galaxy models yet in fact be so rare. Spoke-like features are found in perhaps three of the 40 known ring galaxies, though nowhere near as clearly defined as the Cartwheel's.

4.5. *Which Companion Is the Intruder?*

The intruder galaxy's identity is essential for a better understanding of the Cartwheel's evolution. For example, the amplitude of the ring density wave and the strength of orbit crowding—factors that directly influence the duration
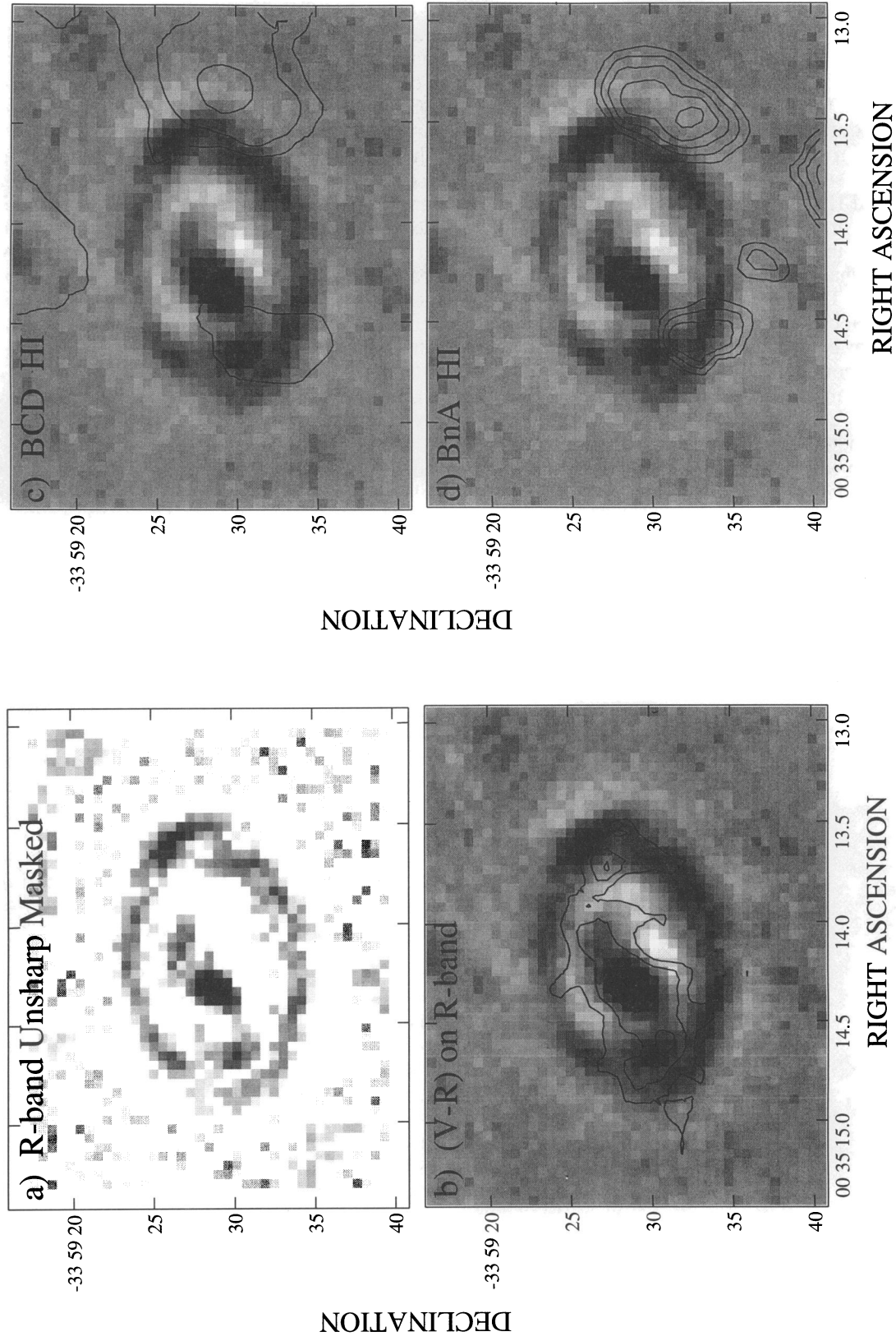
FIG. 16.—Evidence for dust lanes crossing the Cartwheel's inner ring. (*a*) Unsharp-masked inner 30″ of an *R*-band CCD image of the Cartwheel, showing breaks in the inner ring near its major axis. (*b*) Contours of (*V* − *R*) superposed on an *R*-band CCD image of the same region. Contour levels correspond to (*V* − *R*) of 0.98, 1.03, 1.09, 1.14, and 1.21, with the reddest colors found in the nucleus. The spatial resolution in the maps is 1″.6 FWHM. (*c*) Contours of $\Sigma_{\mathrm{H\,I}}$ (BCD) superposed on the *R*-band image. (*d*) Contours of $\Sigma_{\mathrm{H\,I}}$ (BnA), showing the accumulation of H I just outside the inner ring. Neutral gas is associated with both dust features.

and intensity of star formation—depend on the intruder's mass and speed. The choice of intruder is made uncertain by the fact that all three show signs of interaction in their optical or radio morphologies (see Fig. 1 [*insert*] and Fig. 3*b*), and all three lie along the ring's minor axis, as expected of small impact parameter collisions (Theys & Spiegel 1977). Moreover, no optical bridge between the Cartwheel and companions G1 and G2 is present above $\mu_V = 25.8$ mag arcsec^{-2} in the smoothed (3″ FWHM) stack of CCD images shown in the insert in Figure 1, nor is there any evidence of starlight suggesting a link with G3 to the northeast. However, the broad H I plume extending north of the Cartwheel provides the first clear link between the ring galaxy and a companion, in this case G3. A smoothed (20″ FWHM) version of the channel map centered on 8808 km s^{-1} is shown in Figure 17. The gas plume projects very near G3's position, and the velocity range of this feature is closer to G3 than G1, the other companion with H I. Moreover, G3's H I distribution is considerably more distorted than that of G1. Additionally, unlike the case of G1, a companion is not apparent. No connection is seen between the plume and G1's H I in the channel maps, nor is H I found between them at intermediate velocities, as would be expected if the gas was tidal in origin. On the other hand, new hydrodynamic models of Cartwheel-like systems produce broad gas plumes that greatly resemble the distribution seen in Figure 17 (Struck 1995). Gas in the pro-

genitor ring galaxy that overlaps the intruder's disk is ejected out of the plane. The relative speed of the intruder's passage, and the orientation of its disk relative to that of the target, influences the extent and direction of the "splash." The energy required to eject this mass of gas is lost to the intruder's orbit, which results in a modified trajectory, which can account for the observed difference between the V_{sys} of G3 and the plume. Detailed hydrodynamic models of the Cartwheel group in which we specifically model this H I "splash" are in preparation (Struck & Higdon 1996).

The outer ring's radius and V_{exp} imply that ~ 300 Myr has elapsed since the intruder's passage. This timescale can provide a consistency check: Could G3 have traveled to its current position in this time without requiring an unreasonable space velocity? The tangential velocity component was estimated by simply dividing the projected separation between G3 and the Cartwheel (88 kpc) by 300 Myr, while the radial component was taken to be the difference in their V_{sys} (210 km s^{-1}). The resulting space velocity is 360 km s^{-1}, which is not extreme. The fact that the plume occupies one velocity channel means that the intruder's trajectory was nearly in the plane of the sky and that its passage was inclined $\sim 40°$ from the Cartwheel's rotation axis.

Finally, companion G2 can be ruled out as the intruder on the basis of hydrodynamic models, since gas-poor spheroidal galaxies seem unable to generate gas plumes (Struck 1995). Nevertheless, its faint tidal tail ($\mu_V < 25.4$ mag arcsec^{-2}) and pronounced off-centered nucleus apparent in the insert in Figure 1 indicate an ongoing tidal interaction. Their distorted morphologies, close proximity, and the lack of an obvious optical or H I bridge to the ring galaxy, point to G1 and G2 being a *separate* interacting pair in the Cartwheel Group, with no direct influence on the Cartwheel.

The fate of gas in the plume depends on whether or not it has attained escape velocity relative to the Cartwheel. Using M_{ind} of $3 \times 10^{11} M_\odot$ from § 3.2.2 and a relative speed of the plume of 280 km s^{-1}, V_{esc} is reached roughly 33 kpc (1′3 in projection) from the ring galaxy. At least half of the plume's mass exists at or beyond this distance, which implies that much of this gas will escape the ring galaxy. The lower mass H I clumps present in channels 8552–8743 km s^{-1} may very well represent gas returning to the Cartwheel's disk.

4.6. *The Precollision Cartwheel*

Properties of the precollision Cartwheel can be derived from the optical and radio data. For instance, the ring's small optical nucleus and lack of a prominent bulge implies that it was originally a late spiral, probably similar in appearance to G1. Ring galaxies with prominent bulges are known (e.g., AM 0644−741; Few et al. 1982), which shows that this component is not significantly modified by the interaction. Further, neglecting the starburst outer ring, the Cartwheel and G1 have comparable red continuum fluxes (Paper I). The low metal abundances and large integrated $EW_{H\alpha}$ are strong evidence for this being the first major episode of MSF at the radius of the ring (Paper I; FH). However, some MSF activity had taken place prior to the collision, as colors and spectra from the inner ring and nucleus indicate evolved stellar populations considerably older than 300 Myr (FH; Marcum et al. 1992). The precollision Cartwheel was not an intergalactic cloud. Instead, the available evidence points to what would appear visually as a small spiral embedded in an extensive low $\Sigma_{H I}$ disk, much like Malin 1 (van Gorkom 1995). The subcritical gas disk
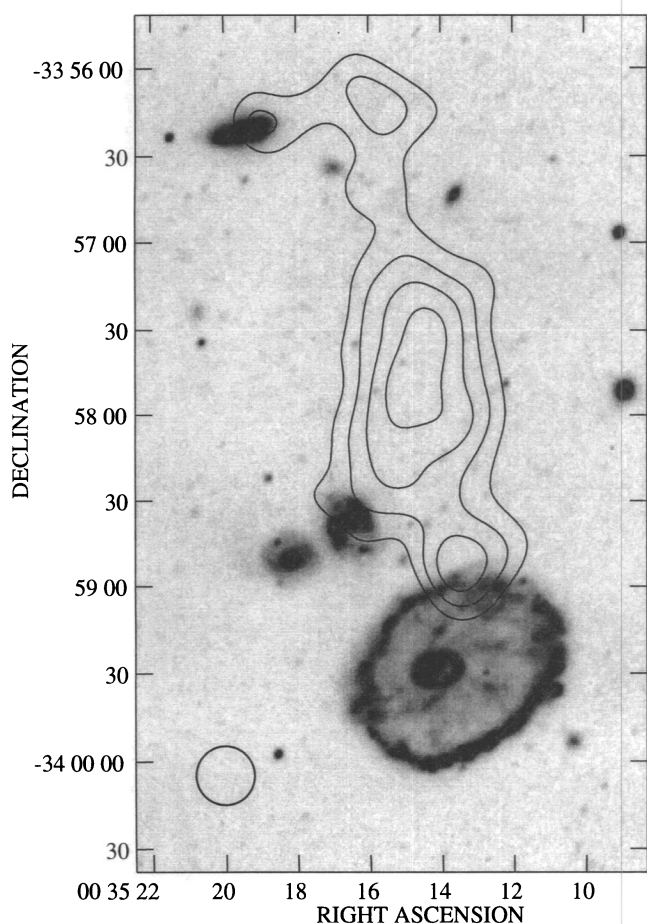

FIG. 17.—A smoothed (20″ FWHM Gaussian) version of the $V = 8808$ km s^{-1} channel map, showing H I linking the ring galaxy and companion G3. The contours are 3, 4, 5, and 6 times the 1 σ map noise of 0.14 mJy beam^{-1}.

prevented robust MSF and chemical enrichment over the disk's lifetime. Approximately 300 Myr ago, companion galaxy G3 passed through the Cartwheel near the nucleus on a trajectory inclined $\sim 40°$ from the rotation axis. The face-on collision between the two disks splashed out $\sim 2 \times 10^9 \ M_\odot$ of gas out of the Cartwheel's plane along the line of sight. The energy required to accelerate this much mass was lost to G3's orbit, which is now traveling on a slightly different trajectory from the H I plume. As a result of its passage, a ring density wave formed and propagated through the subcritical H I disk, triggering high rates of MSF in the metal-poor regions. We presently see the Cartwheel where the ring has either just reached or passed the original extent of the H I disk. Gas and dust are now returning to the inner regions, though MSF in the inner ring will probably require the accumulation of another $\sim 8 \times 10^8 \ M_\odot$ of gas. A significant fraction of the Cartwheel's H I was removed from the disk by G3's passage. The above analysis indicated that much of this material will return to the disk. Even with the addition of another $\sim 10^9 \ M_\odot$ of H I, a sustained starburst triggered by the inner ring, or another 300 Myr of intense MSF by the outer ring, the Cartwheel will be transformed into an anomalously blue but gas-poor disk galaxy. This system provides a striking example of galaxy transformation through collisions.

5. CONCLUSIONS

The VLA was used in multiple configurations to study the H I and radio continuum properties in the Cartwheel ring galaxy, with the goals of better understanding its kinematics, and the relationship between neutral atomic gas and MSF. The results of this study are as follows:

1. The Cartwheel possesses $9.3 \times 10^9 \ M_\odot$ of H I, roughly 60% of the group's total. Of this amount, $8.0 \times 10^9 \ M_\odot$ (85%) exists in a clumpy distribution corresponding to the optical outer ring, with $\Sigma_{H I} \approx 5–28 \ M_\odot \ pc^{-2}$. A low $\Sigma_{H I}$ ($\lesssim 4.5 \ M_\odot \ pc^{-2}$) component fills much of the disk interior to the outer ring. Structure is apparent; however, no H I counterparts to the optical "spokes" were found. While the ring galaxy nucleus and inner ring are H I poor, H I appears to be accumulating at the inner ring. There is no evidence of an H I disk beyond the outer ring.

2. Noncircular motions are apparent in the Cartwheel's H I velocity field. Models of expanding and rotating circular rings were successfully fitted to a series of elliptical annuli throughout the ring galaxy. For the outer ring ($R = 16.9$ kpc), $V_{sys} = 9089 \pm 5 \ km \ s^{-1}$, $V_{cir} = 291 \pm 9 \ km \ s^{-1}$, and $V_{exp} = 53 \pm 9 \ km \ s^{-1}$. The outer ring's radius and V_{exp} imply that $\sim 313 \pm 48$ Myr have elapsed since the intruder's passage. Solid body rotation is apparent throughout the disk. Radial changes in V_{exp} shows that H I interior to the outer ring is starting to fall back to smaller radii. For $R \lesssim 8$ kpc, V_{exp} is negative.

3. H I was detected in companion galaxies G1 ($M_{H I} = 2.7 \times 10^9 \ M_\odot$) and G3 ($M_{H I} = 0.7 \times 10^9 \ M_\odot$). The distribution of H I in G3 is distorted. From their total H I line widths or optical velocity dispersion, the companion galaxy's M_{ind} were all found to be $\lesssim 6\%$ of the Cartwheel's. Extensive low $\Sigma_{H I}$ is apparent in the channel centered on 8808 km s^{-1}. Smoothing reveals a massive H I plume ($2 \times 10^9 \ M_\odot$) projecting 88 kpc from the Cartwheel toward G3. Spatial and velocity continuity arguments lead to its identification as gas "splashed out" of the Cartwheel's disk

by the passage of G3. Much of this material has attained V_{esc} for the Cartwheel, but significant amounts appear to be infalling onto the disk.

4. Radio continuum emission at 20 cm is greatly enhanced in the outer ring and shows the same azimuthal structure seen in Hα. A Type II supernova rate of 0.1 ± 0.02 yr^{-1} was derived using the 20 cm flux, which agrees with the lower bound of optical estimates. Maps at 6 cm show only two point sources, both in the outer ring. The brightest corresponds with the most luminous H II complex (CW 17). Scaled-array 6 cm–20 cm spectral indices of -0.6 ± 0.2 and -0.7 ± 0.3 were derived for the two sources, indicating a strong nonthermal component. An average 6 cm–Hα A_V of 1.9 ± 0.2 was derived, in reasonable agreement with A_V derived using optical line ratios, although the former is almost certainly an upper limit.

5. H II complexes are found adjacent to H I clumps and tend to lie slightly *beyond* the H I ring throughout much of the starburst southern quadrant. This is consistent with MSF triggered near the outer edge of a gas ring density wave. If the inner ring triggers a sustained starburst similar to the outer ring's, the Cartwheel's gas supply could be largely consumed in another ~ 300 Myr. The neutral ISM is significantly depleted in the southern quadrant.

6. Neutral atomic gas in the Cartwheel's low $\Sigma_{H I}$ disk is below the critical threshold for star formation as formulated by Kennicutt (1989), which can account for the absence of detectable of MSF. Only in the outer ring is the threshold exceeded. However, a pronounced anticorrelation between $\Sigma_{H I}$ and $\Sigma_{H\alpha}$ in the ring suggests that local effects have a more direct bearing on MSF. A Schmidt law relationship between MSF and atomic gas surface density is not apparent in the outer ring. The amount of molecular gas required to recover a Schmidt law has not been detected from ^{12}CO (1–0) observations.

7. Most of the predictions of recent models of Cartwheel-like systems are wrong. The spokes are *not* rich in H I or H II. MSF is clearly dominated by the outer rings in all ring galaxies studied to date, and the analysis of radial color gradients will not be significantly affected by ongoing MSF in the disk. Shear or high temperatures may be responsible for retarding MSF in the spokes and disk. An extensive low column density gas disk appears to be required to produce the ring's large $\Sigma_{H I}$.

8. Small H I line widths in the outer ring argue against a starburst triggered by disruptive cloud collisions (Olson & Kwan 1990). Instead, the ring appears to concentrate the ISM into a very dense environment sufficiently long ($\gtrsim 40$ Myr) to form very massive clouds through agglomeration. The situation is reminiscent of the models of Scalo & Struck-Marcell (1986), in which a burst mode is attained for high cloud collision rates. The initial density distribution and feedback from massive stars may also affect the distribution of MSF in the ring.

9. The available evidence indicates that the Cartwheel was originally a small late spiral with an extensive low column density gas disk. Approximately 300 Myr ago, companion galaxy G3 passed through its disk on a low impact parameter trajectory, "splashing" out $\sim 2 \times 10^9 \ M_\odot$ of H I and initiating a propagating burst of MSF—the first significant one in the disk's history. Another ring triggered burst may exhaust the remaining gas supply, meaning that the Cartwheel will appear as an anomalously blue, but gas-poor, disk galaxy in $\lesssim 0.6$ Gyr.

REFERENCES

Appleton, P. N. A., & Struck-Marcell, C. 1987, ApJ, 318, 103 (ASM)
Baars, J. W. M., Genzel, R., Pauliny-Toth, I. I. K., & Witzel, A. 1977, A&A, 61, 99
Balkowski, C. 1973, A&A, 29, 43
Benedict, G. F., & Shelus, P. 1978, in IAU Colloq. 48, Modern Astrometry, ed. F. Prochazka & R. H. Tucker (Vienna: Institute of Astronomy), 109
Bessel, M. S. 1979, PASP, 91, 589
Bloemen, J. B. G. M., et al. 1986, A&A, 154, 25
Brinks, E. 1990, in The Interstellar Medium of Galaxies, ed. H. Thronson & J. Shull (Dordrecht: Kluwer), 39
Buta, R. J. 1986, ApJS, 61, 631
Caldwell, N., Kennicutt, R. C., Phillips, A. C., & Schommer, R. A. 1991, ApJ, 370, 526
Caswell, R. 1970, A&A, 7, 59
Charmandaris, V., Appleton, P. N., & Marston, A. P. 1993, ApJ, 414, 154
Christian, C. A., Adams, M., Barnes, J. V., Butcher, H., Hayes, D. S., Mould, J. R., & Siegel, M. 1985, PASP, 97, 363
Clark, B. G. 1980, A&A, 89, 337
Condon, J. J., & Yin, Q. F. 1990, ApJ, 357, 97
Davies, R. D., Elliot, K. H., & Meaburn, J. 1976, MNRAS, 81, 89
Davies, R. L., & Morton, D. C. 1982, MNRAS, 201, 69P
de Vaucouleurs, G. 1958, ApJ, 128, 465
Few, J. M. A., Madore, B. F., & Arp, H. J. 1982, MNRAS, 199, 633
Fosbury, R. A. E., & Hawarden, T. G. 1976, MNRAS, 178, 473 (FH)
Franco, J., & Cox, D. P. 1986, PASP, 98, 1076
Gebel, W. L. 1968, ApJ, 153, 743
Hernquist, L., & Weil, M. L. 1993, MNRAS, 261, 804 (HW93)
Higdon, J. L. 1995, ApJ, 455, 524 (Paper I)
Higdon, J. L., Lord, S. D., & Rand, R. J. 1996, in preparation
Higdon, J. L., & Wallin, J. F. 1996, submitted
Horellou, C. 1995, A&A, 289, 743

Jeske, N. A. 1986, Ph.D. thesis, Univ. of California, Berkeley
Kaufman, M., Bash, F. N., Kennicutt, R. C., & Hodge, P. W. 1987, ApJ, 319, 61
Kennicutt, R. C. 1983, ApJ, 272, 54
———. 1989, ApJ, 344, 685
Marcum, P. M., Appleton, P. N. A., & Higdon, J. L. 1992, ApJ, 399, 57
Marston, A., & Appleton, P. N. 1995, AJ, 109, 1002
Mebold, U., Goss, W. M., & Fosbury, R. A. E. 1977, MNRAS, 180, 11P
Mihos, J. C., & Hernquist, L. 1994, ApJ, 437, 611 (MH94)
Miller, J. S., & Mathews, W. G. 1972, ApJ, 172, 593
Olson, K. M., & Kwan, J. 1990, ApJ, 349, 480
Safronov, V. S. 1960, Ann. d'Astrophys., 23, 979
Scalo, J. M., & Struck-Marcell, C. 1986, ApJ, 301, 77
Struck, C. 1995, private communication
Struck, C., & Higdon, J. L. 1996, in preparation
Struck-Marcell, C., & Higdon, J. L. 1993, ApJ, 411, 108 (SMH)
Taylor, K., & Atherton, P. D. 1984, MNRAS, 208, 601
Theys, J. C., & Spiegel, E. A. 1977, ApJ, 212, 616
Toomre, A. 1964, ApJ, 139, 1217
———. 1977, in IAU Symp. 79, The Large Scale Structure of the Universe, ed. M. S. Longair & J. Einasto (Dordrecht: Reidel), 109
van der Hulst, J. M., Kennicutt, R. C., Crane, P. C., & Rots, A. H. 1988, A&A, 195, 38
van der Hulst, J. M., Skillman, E., Kennicutt, R. C., & Bothun, G. 1987, A&A, 177, 63
van der Kruit, P. C. 1974, ApJ, 188, 3
van Gorkom, J. H. 1995, private communication
Vogel, S. N., Kulkarni, S. R., & Scoville, N. Z. 1988, Nature, 334, 402
Wallin, J. F., & Struck-Marcell, C. 1994, ApJ, 433, 631
Young, J. S., Xie, S., Kenney, J. D. P., & Rice W. L. 1989, ApJS, 70, 699